Wang et al. *Zool. Res.* 2025, 46(4): 877−892
https://doi.org/10.24272/j.issn.2095-8137.2025.035
https://cstr.cn/32248.14.zr.2025.035

ZR Zoological Research

Article Open Access

Anatomical mapping of GFAP-immunoreactive astrocytes in the tree shrew brain

Ya-Tao Wang[1,2,#], Qi-Qi Xu[1,2,#], Shuo-Wen Wang[1,2], Jin-Kun Guo[2], Shuai-Deng Wang[1,2], Xin-Ya Qin[2], Qing-Hong Shan[2], Yu Wang[2], Rong-Yu Liu[3], Yue-Xiong Yang[4], Chen-Wei Wang[1], Peng Chen[1,2,5,*], Jiang-Ning Zhou[2,5,6]

[1] *Department of Anatomy*, *School of Basic Medical Sciences*, *Anhui Medical University*, *Hefei*, *Anhui* 230032, *China*
[2] *Institute of Brain Science*, *The First Affiliated Hospital of Anhui Medical University*, *Hefei*, *Anhui* 230022, *China*
[3] *Anhui Geriatrics Institute*, *The First Affiliated Hospital of Anhui Medical University*, *Hefei*, *Anhui* 230022, *China*
[4] *Key Laboratory of Animal Models and Human Disease Mechanisms*, *Laboratory of Learning and Memory*, *Center for Excellence in Brain Science and Intelligence Technology*, *Kunming Institute of Zoology*, *Chinese Academy of Sciences*, *Kunming*, *Yunnan* 650223, *China*
[5] *Anhui Provincial Key Laboratory for Brain Bank Construction and Resource Utilization*, *Anhui Medical University*, *Hefei*, *Anhui* 230032, *China*
[6] *Center for Excellence in Brain Science and Intelligence Technology*, *Chinese Academy of Sciences*, *Shanghai* 200031, *China*

ABSTRACT

Astrocytes are associated with varying brain size between rodents and primates. As a close evolutionary relative of primates, the tree shrew (*Tupaia belangeri*) provides a valuable comparative model for investigating glial architecture. However, the anatomical distribution and morphological characteristics of astrocytes in the tree shrew brain remain poorly characterized. In this study, glial fibrillary acidic protein (GFAP) immunofluorescence was employed to systematically examine the spatial distribution and morphology of astrocytes in the whole brain of tree shrews. Notably, GFAP-immunoreactive (ir) astrocytes were detected throughout the telencephalon, diencephalon, mesencephalon, metencephalon, and myelencephalon. Distinct laminar distribution was evident in regions such as the main olfactory bulb and hippocampus. Semi-quantitative comparisons revealed significant regional differences in astrocyte density between tree shrews and mice, encompassing the main olfactory bulb, accessory olfactory bulb, olfactory tubercle, cortex, hippocampus, cortical amygdaloid nucleus, hypothalamus, thalamus, superior colliculus, interpeduncular nucleus, median raphe nucleus, and parabrachial nucleus. Compared to mice, tree shrews exhibited higher astrocyte density with increased morphological complexity in the posterior hypothalamic nucleus, dorsomedial hypothalamic nucleus, ventromedial hypothalamic nucleus, and periaqueductal gray, but lower density with greater morphological complexity in the hippocampus and substantia nigra. In the paraventricular hypothalamic nucleus and lateral hypothalamic area, GFAP-ir astrocytes displayed comparable densities between tree shrews and mice but exhibited region-specific differences in morphological complexity. This study provides the first brain-wide mapping of GFAP-ir astrocytes in tree shrews, revealing marked interspecies differences in their distribution and morphology, and establishing a neuroanatomical framework for understanding astrocyte involvement in diverse physiological and behavioral functions.

Keywords: Tree shrews; Astrocytes; Morphology; Hippocampus; Hypothalamus

INTRODUCTION

Astrocytes, a major class of glial cells, are widely distributed throughout the vertebrate brain (Endo et al., 2022; Zhou et al., 2019) and perform a diverse array of essential functions, including maintenance of the blood-brain barrier (Abbott et al., 2006; Manu et al., 2023), orchestration of synaptogenesis (Irala et al., 2024; Lawal et al., 2022; Stogsdill et al., 2017), regulation of ion homeostasis (Hertz & Chen, 2016), buffering of neurotransmitters (Andersen et al., 2022; Cahill et al., 2024), and secretion of neuroactive substances (Verkhratsky et al., 2016). Astrocytes also exhibit complex morphologies, characterized by dense branches and branchlets, which form well- delineated territories (Khakh & Sofroniew, 2015; Zhou et al., 2019). From the cell soma, primary branches extend

---

Received: 02 April 2025; Accepted: 25 April 2025; Online: 26 April 2025

Foundation items: This work was supported by the STI2030-Major Projects (2022ZD0205202), Anhui Provincial Natural Science Foundation (2408085Y043), and National Natural Science Foundation of China (82471540, 32030046, 32200798)

[#] Authors contributed equally to this work

[*] Corresponding author, E-mail: pchen727@ustc.edu.cn

radially and gradually bifurcate into intricate networks of fine terminal processes, many of which exhibit a high degree of binding to synapses (Cheng et al., 2023; Freeman, 2010). The structural complexity of astrocytes, as well as the spatial proximity of astrocytic leaflets to the synaptic cleft, varies significantly across brain regions and mammalian taxa, and is known to undergo profound remodeling in response to pathological insults (Baldwin et al., 2024; Falcone, 2022; Khakh & Sofroniew, 2015; Oberheim et al., 2009). Comparative studies have revealed that astrocytes in primates are not only more numerous but also morphologically larger than those in rodents (Heffernan et al., 2024). In the human cerebral cortex, astrocytes display greater structural diversity, enhanced complexity, and more rapid calcium signaling dynamics than their rodent counterparts (Falcone et al., 2019; Oberheim et al., 2009, 2012). Investigating astrocytes in primates may yield deeper insights into the cellular mechanisms underlying human disease pathogenesis.

The tree shrew (*Tupaia belangeri*), a small-bodied, easily bred mammal with rapid reproductive capacity, has emerged as a promising experimental animal due to its close genetic proximity to primates (Xiao et al., 2017; Yao et al., 2024). Its anatomical, neurodevelopmental, and stress-related psychological traits exhibit a high degree of similarity to those of primates, including humans (Liu et al., 2023; Xiao et al., 2017), highlighting its value in studies related to a broad spectrum of human diseases, including infectious, oncological, psychiatric, ophthalmological, metabolic, and immune-related disorders (Fuchs, 2005; Lu et al., 2021; Ni et al., 2018; Tsukiyama-Kohara & Kohara, 2014; Xiao et al., 2017; Yao, 2017). Despite increasing use of the tree shrew in biomedical research, a foundational understanding of its neural cell architecture remains incomplete—particularly with respect to glial cell populations. While numerous studies have characterized the distribution, projections, and functions of neuronal subtypes within the tree shrew brain (Duan et al., 2022; Huang et al., 2020; Lu et al., 2016; Ni et al., 2014, 2015, 2016, 2021a, 2021b; Nie et al., 2024; Shu et al., 2015), knowledge of astrocyte biology in this species remains limited. Prior investigations have offered only fragmentary insights. For instance, an early investigation reported that astrocytes lacking long processes are primarily located in the superficial layers of the dorsolateral cortex in tree shrews (Colombo et al., 2000). Subsequent work in the primary visual cortex demonstrated that astrocytic oxidative metabolism is tightly coupled to glutamatergic neurotransmission (Sonnay et al., 2018). In the hippocampus, chronic psychosocial stress elicits a pronounced reduction in both astrocyte number and soma volume, although fluoxetine treatment effectively blocks the decline in cell number without reversing soma shrinkage (Czéh et al., 2006). While these studies have provided valuable insights into region-specific astrocyte responses, they remain limited to discrete cortical and hippocampal areas. A comprehensive characterization of astrocyte distribution and morphology across the entire tree shrew brain has not yet been reported.

This study addressed the existing knowledge gap through glial fibrillary acidic protein (GFAP) immunofluorescence combined with whole-brain morphological reconstruction in the tree shrew. Astrocytic features were systematically identified in the telencephalon, diencephalon, mesencephalon, metencephalon, and myelencephalon, with parallel comparative analyses conducted in mice. The results revealed region- and layer-specific distribution of GFAP-immunoreactive (ir) astrocytes throughout the tree shrew brain. Notably, astrocyte density and morphological complexity varied in a region-dependent manner between tree shrews and mice. This work provides the first comprehensive anatomical atlas of astrocytes in the tree shrew and offers key insights into the evolutionary diversification of astroglia, reinforcing the translational utility of this species in neurodevelopmental and neuropathological research.

MATERIALS AND METHODS

Animals

Five adult male tree shrews (*Tupaia belangeri*) (8 months) from the breeding colony in the Animal House Center of the Kunming Institute of Zoology (China) and six adult male C57BL/6J mice (8–10 weeks) were used in this study. The tree shrews and mice were housed individually in animal facilities under a temperature of 24±2℃ and a 12 h light/dark cycle (light on at 0800h) with food and water available *ad libitum*. All animal procedures and handling were approved by the Institutional Animal Care and Use Committee of Anhui Medical University (approval no. LLSC20241768). All efforts were made to minimize animal suffering as well as the number of animals used.

Tissue preparation

The tree shrews and mice were deeply anesthetized with pentobarbital sodium (80 mg/kg, intraperitoneal), then perfused with saline followed by 4% paraformaldehyde in phosphate-buffer (0.1 mol/L; pH 7.4). After perfusion, the brains were removed and post-fixed by immersion in the same fixative overnight at 4℃. The brains from three tree shrews and four mice were soaked in 15% sucrose in phosphate-buffered saline (PBS: 0.1 mol/L; pH 7.4) until the tissues sank, followed by soaking in 30% sucrose solution in PBS. The brains were then frozen and sectioned into serial slices (30 μm thick) on a cryostat microtome (RWD Life Science, China). Sections were stored at –20℃ until use. Brains from one tree shrew and one mouse were sectioned into serial slices (100 μm thick) on a vibrating microtome (B-S-1018, Bitelligen, China). Sections were stored at 4℃ until use.

Immunofluorescent staining

For GFAP immunofluorescence, brain sections (30 μm or 100 μm thick) were rinsed and permeabilized with 0.5% Triton X-100 in PBS (PBST) for 1 h. Sections (100 μm thick) were then blocked with 5% normal donkey serum (017-000-121, Jackson ImmunoResearch, USA) in 0.5% PBST at room temperature for 1 h, followed by incubation with either rabbit polyclonal anti-GFAP (Z0334, Dako, 1:1 000, Denmark) or mouse monoclonal anti-GFAP (G3893, Sigma-Aldrich, 1:500, USA) primary antibodies in 0.5% PBST at 4℃ for 24 h or 48 h. Subsequently, sections (100 μm thick) were rinsed and incubated with donkey anti-rabbit IgG-conjugated Alexa Fluor 594 (711-585-152, Jackson ImmunoResearch, 1:200) or donkey anti-mouse IgG-conjugated Alexa Fluor 594 (715-585-151, Jackson ImmunoResearch, 1:200, USA) secondary antibodies at room temperature for 2 h or 4℃ for 12 h. The sections were then rinsed and incubated with 4’,6-diamidino-2-phenylindole dihydrochloride (DAPI; D1306, Thermo Fisher Scientific, 1:2 000, USA) at room temperature for 30 min. Finally, sections were rinsed and coverslipped with glycerin. Specificity of GFAP labeling was verified using a negative control in which the anti-GFAP primary antibody was omitted and the secondary antibody was applied.

For dual-immunofluorescence, sections were rinsed and permeabilized with 0.5% PBST for 1 h, followed by blocking with 5% normal donkey serum (Jackson ImmunoResearch, USA) in 0.5% PBST at room temperature for 1 h. Sections were then incubated with primary antibodies at 4℃ for 48 h, including rabbit polyclonal anti-GFAP (Z0334, Dako, 1:1 000, Denmark), mouse monoclonal anti-neuron-specific nuclear protein (anti-NeuN, MAB377, Millipore, 1:1 000, USA), rat monoclonal anti-ionized calcium binding adaptor molecule 1 (anti-Iba1, ab283346, Abcam, 1:500, UK), mouse monoclonal anti-myelin oligodendrocyte glycoprotein (anti-MOG, ab243034, Abcam, 1:500, UK), and mouse monoclonal anti-α-smooth muscle actin (anti-α-SMA, 67735-1-lg, Proteintech, 1:500, USA). Following primary antibody incubation and rinsing, sections were incubated with secondary antibodies at room temperature for 2 h, including Alexa Fluor 594-conjugated donkey anti-rabbit IgG (1:200), Alexa Fluor 488-conjugated donkey anti-rat IgG (711-545-153, Jackson ImmunoResearch, 1:200, USA), and Alexa Fluor 488-conjugated donkey anti-mouse IgG (715-545-150, Jackson ImmunoResearch, 1:200, USA). Sections were subsequently rinsed and incubated with DAPI (1:2 000) at room temperature for 30 min, then rinsed and coverslipped with glycerin. The stained sections were imaged using a confocal laser-scanning microscope (Spin SR, Olympus, Japan) under a 20× or 60× objective. A summary of the distribution of GFAP-ir astrocytes throughout the brains of tree shrews and mice is provided in Supplementary Table S1.

Immunohistochemistry

Briefly, sections (30 μm thick) were treated with 0.3% hydrogen peroxide in 0.5% PBST for 1 h. Antigen retrieval was performed in citrate buffer for 20 min, after which the sections were blocked with 5% normal goat serum (005-000-121, Jackson ImmunoResearch, USA) in 0.5% PBST at 37℃ for 1 h. Sections were then incubated with rabbit polyclonal anti-GFAP (Z0334, Dako, 1:1 000, Denmark) or mouse monoclonal anti-GFAP (G3893, Sigma-Aldrich, 1:500, USA) for 24 h at 4℃, followed by incubation with biotinylated goat anti-mouse IgG (BA-9200, Vector Laboratories, 1:200, USA) or goat anti-rabbit IgG (BA-1000, Vector Laboratories, 1:200, USA) and avidin-biotin peroxidase complex (PK-4000, Vector Laboratories, 1:200, USA). Sections were stained with 0.05% 3,3′-diaminobenzidine (Sigma-Aldrich, USA) and 0.25% $NiSO_4 \cdot 6H_2O$ (Sigma-Aldrich, USA) as chromogen. Sections were then dehydrated in a gradient of ethanol, cleared in xylene, and coverslipped using gum.

Western blot analysis

Brain protein extracts were prepared from one tree shrew and one mouse using RIPA solution (Radio-Immunoprecipitation Assay) mixed with a protease inhibitor cocktail (Roche, Switzerland) and phosphatase inhibitor (Roche, Switzerland), following established procedures (Li et al., 2024; Qi et al., 2024). Proteins were separated by 12% sodium dodecyl sulfate-polyacrylamide gel electrophoresis (SDS-PAGE) and transferred for western blot analysis. GFAP was detected using rabbit polyclonal anti-GFAP (Z0334, Dako, 1:1 000, Denmark) or mouse monoclonal anti-GFAP (G3893, Sigma-Aldrich, 1:1 000, USA) and appropriate horseradish peroxidase (HRP)-conjugated secondary antibodies: anti-rabbit IgG (W401B, Promega, 1:2 000, USA) or anti-mouse IgG (W402B, Promega, 1:2 000, USA). Signals were detected with enhanced chemiluminescence (BL520B, Biosharp, Canada) on a chemiluminescence imaging system (Tanon-4600, China).

Astrocyte density quantification in tree shrews and mice

Astrocyte densities were assessed in 10 brain regions from three tree shrews and four mice. Each region was subdivided into rostral (first third), middle (intermediate third), and caudal (last third) parts. For tree shrews, coronal sections were collected at 0.18 mm intervals; for mice, sections were collected at 0.09 mm intervals. In each section, two identical grids were applied bilaterally to the target region, with the number of astrocytes in each grid then counted using ImageJ. Astrocyte density for a region in one section was determined as the mean count from the two grids. Only GFAP-ir cells co-labeled with DAPI-positive signals were included in the analysis. Astrocyte density in the rostral, middle, or caudal subdivision of each region was calculated as the mean density measured across the corresponding sections for that individual. Bregma coordinates for tree shrews were referenced from the tree shrew brain atlas (Zhou & Ni, 2016), and for mice from the Mouse Brain in Stereotaxic Coordinates, 4th edition (Paxinos & Franklin, 2001).

Three-dimensional (3D) reconstruction

To assess astrocytic morphology, GFAP- and DAPI-stained brain sections (100 μm thick) were imaged using a confocal laser-scanning microscope equipped with a 60× objective. Image stacks were obtained at a resolution of 2304×2304 pixels with a z-stack step size of 1.0 μm. All images were captured from the center of each brain structure to minimize overlap with adjacent regions. Identical confocal settings were used, including laser intensity, exposure time, and display adjustments. Imaris v.9.3 (Bitplane, Switzerland) was used to quantify filament length, filament area, and filament volume, as well as to conduct Sholl analysis. Only GFAP-ir astrocytes with fully visualized filamentous processes were selected for reconstruction. The following parameters were applied for astrocytic filament tracing: starting point, 4 μm; seed point, 0.5 μm; smoothing factor, 0.325; sphere diameter, 10.8 μm. In cases where two astrocytes were erroneously identified as a single cell, manual separation was performed using the cut function. Automated reconstructions were manually adjusted. At least seven astrocytes co-labeled with DAPI from the rostral, middle, or caudal parts of each region were selected for reconstruction. Filament data and branching points for each astrocyte were determined using Imaris and used for subsequent Sholl analysis. Image processing, reconstruction, and quantification were performed blind to experimental conditions.

Statistical analysis

GraphPad Prism v.9.0 (GraphPad, USA) was used for statistical analysis and graph generation. Differences among multiple groups were analyzed using one-way repeated measures (RM) analysis of variance (ANOVA), two-way ANOVA, or two-way RM ANOVA, followed by Bonferroni *post hoc* tests. All datasets were checked for normality using the Kolmogorov-Smirnov test and for homogeneity of variance. Detailed statistical results are shown in Supplementary Tables S2, S3. Data are presented as mean±standard error of the mean (SEM), and $P<0.05$ was considered statistically significant.

RESULTS

To evaluate the suitability of GFAP immunostaining in tree shrew and mouse brains, anti-GFAP antibodies from different sources were tested. Both immunostaining and western blotting confirmed that the two anti-GFAP antibodies effectively and specifically labeled GFAP in both species (Supplementary Figure S1). Based on these results, the rabbit polyclonal anti-GFAP antibody (Dako, Z0334) was selected for all subsequent experiments. To further confirm antibody specificity, GFAP immunofluorescence co-staining was performed with NeuN, Iba1, and MOG, respectively (Supplementary Figure S2). Results showed no co-localization of GFAP with any of the three markers. Additionally, no immunofluorescent signal was detected in negative control sections from tree shrew and mouse brains (Supplementary Figure S3). These findings validate both the suitability and specificity of the anti-GFAP antibody used in this study.

GFAP immunoreactivity in each brain region was evaluated using the relative intensity scale depicted in Supplementary Figure S4. GFAP-ir astrocytes exhibiting light, moderate, and intense immunostaining are represented with +, ++, and +++ (Supplementary Figure S4A–C). A summary of the anatomical distribution and relative density of GFAP-ir astrocytes across brain regions in tree shrews and mice is provided in Supplementary Table S1. To facilitate visualization, regional astrocyte distributions were further illustrated using heatmaps (Supplementary Figures S5, S6).

Telencephalon

Rhinencephalon: GFAP-ir astrocytes were unevenly distributed within the main olfactory bulb (MOB) (Figure 1A), accessory olfactory bulb (AOB) (Figure 1B), and anterior olfactory nucleus (AON) (Figure 1C). In the MOB, astrocytes exhibited a prominent laminar distribution. Strong GFAP-ir signals were observed in the ependyma and subependymal layers (E) (Figure 1A4). In addition, GFAP-ir astrocytes were abundant in the olfactory nerve layer (ONL) and glomerular layer of the olfactory bulb (GL) (Figure 1A1, A2). GFAP-ir fibers showed a moderate density in the ONL, with short and scattered processes (Figure 1A1), while astrocytes displayed densely interwoven fibers and clearly defined somata in the GL (Figure 1A1, A2). Sparse astrocytic fibers were present in the external plexiform layer (EPl) (Figure 1A2), internal plexiform layer (IPl) (Figure 1A3), mitral cell layer (MCL) (Figure 1A3), and granule cell layer (GCL) (Figure 1A4) of the olfactory bulb. Similarly, in the AOB, a substantial number of GFAP-ir astrocytes were distributed in the glomerular layer (GlA) (Figure 1B1), external plexiform layer (EPlA) (Figure 1B2), and granule cell layer of the accessory olfactory bulb (GrA) (Figure 1B4) but showed sparse to moderately dense distribution in the mitral cell layer of the accessory olfactory bulb (MiA) (Figure 1B3). In contrast, the AON exhibited no detectable GFAP-ir signals (Figure 1C, C1–C4).

Neocortex: GFAP-ir astrocytes showed a laminar distribution in the neocortex of tree shrews (Figure 1D). Layer I contained a high density of GFAP-ir astrocytes (Figure 1D, D1), with clearly defined cell bodies and vertically oriented fibers occasionally observed extending into deeper layers (Figure 1D, D1). In layers II–VI, GFAP-ir astrocytes were sparsely distributed in the perivascular region (Supplementary Figure S7). Moderate densities of astrocytes were detected in the cingulate cortex (Cg) (Figure 1E), entorhinal cortex (Ent) (Figure 1F), and ectorhinal cortex (Ect) (Figure 1F). In these regions, GFAP-ir astrocytes with irregular somata and abundant fibers were primarily located near the cortical edge and exhibited disorganized spatial arrangements. In the piriform cortex (Pir), GFAP-ir astrocytes were confined to layer I, with no signal detected in layers II/III (Figure 1E).

Hippocampus: Immunofluorescence staining of coronal sections revealed the full rostrocaudal extent of the hippocampal formation in tree shrews, situated beneath the cortex (Figure 2A–F). Astrocytes initially emerged on the ventral side of the brain, then exhibited a gradual increase in density, with a laminar distribution in the dentate gyrus (DG), cornu ammonis 3 (CA3), and cornu ammonis 1 (CA1) regions (Figure 2A–F).

In the polymorphic cell layer of the dentate gyrus (PoDG), GFAP-ir astrocytes were tightly packed, exhibiting thick and densely interwoven fibers. The molecular layer (MoDG) showed sparse to moderate astrocyte density, while the granular cell layer (GrDG) lacked detectable GFAP immunoreactivity (Figure 2D1, D2). In CA3, GFAP-ir astrocytes were sparsely to densely distributed in the stratum radiatum (Rad) and lacunosum moleculare (LMol) (Figure 2D2, D3) and sparsely to moderately distributed in the stratum oriens (Or) (Figure 2D3). No GFAP-ir astrocytes were observed in the stratum pyramidal cell layer (Py; Figure 2D3). In CA1, the Rad and LMol showed sparse to moderate astrocyte densities, characterized by conspicuous somata with short, radial fibers. No GFAP-ir astrocytes were observed in the Py layer of the CA1 (Figure 2D4).

Overall, GFAP-ir astrocytes were widely distributed across the DG, CA3, and CA1 regions of the hippocampus. High astrocyte densities were observed in the Rad and LMol of CA3 and in the PoDG. Moderate densities were detected in the LMol, Rad, and Or of CA1 as well as in the MoDG. No GFAP-ir astrocytes were present in the GrDG or Py layers.

Basal ganglia: GFAP-ir astrocytes were sparsely distributed within the accumbens nucleus (Acb), striatum (CPu) and ventral pallidum (VP) (Figure 3A, B). In contrast, a substantial number of GFAP-ir astrocytes were observed in the internal capsule (ic), a white matter region separating the CPu into the caudate (Cd) and putamen (Pu) (Figure 3B). In the globus pallidus (GP), a large number of GFAP-ir astrocytes were detected with clear somata and dense intertwined fibers (Figure 3B). No GFAP-ir astrocytes were present in the claustrum (Cl) (Figure 3B).

Amygdala: Within the amygdaloid complex, GFAP-ir astrocytes were occasionally observed at high density in the anterior cortical amygdaloid nucleus (Aco) (Figure 3C). Sparse to moderate astrocyte densities were found in the medial nucleus (MeA), sublenticular extended amygdala (EA), and basolateral nucleus (BLA) (Figure 3D). Moderately dense astrocyte populations were evident in the central nucleus (CeA), anterior amygdaloid area (AA), and Aco (Figure 3D). Interestingly, astrocytes in these regions were predominantly located in the perivascular zone (Supplementary Figure S7). No GFAP-ir astrocytes were detected in the amygdalohippocampal area (AHi) (Figure 3E).

Septal and preoptic regions: Coronal immunofluorescence revealed the distribution of GFAP-ir astrocytes across the septal nucleus of the tree shrew from rostral to caudal (Figure 3F–H). High astrocyte densities were observed in the medial preoptic area (MPA), median preoptic nucleus (MnPO), and triangular septal nucleus (TS) (Figure 3G–I). Moderately to highly dense GFAP-ir astrocytes were also detected in the

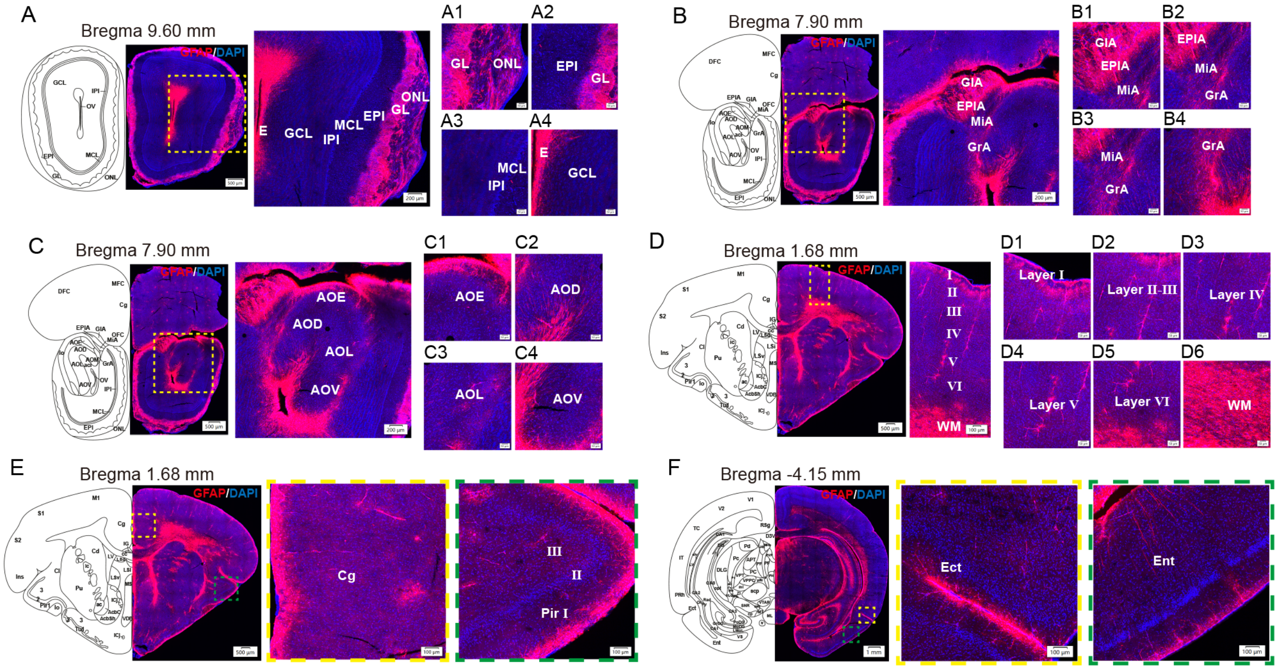

Figure 1 GFAP immunoreactivity in the rhinencephalon and neocortex

A–C: Representative images showing GFAP immunoreactivity (red) co-labeled with DAPI (blue) in the MOB (A), AOB (B), and AON (C) of the tree shrew brain. D: Representative images showing GFAP immunoreactivity (red) co-labeled with DAPI (blue) in different layers of the neocortex in the tree shrew brain. E, F: Representative images showing GFAP immunoreactivity (red) co-labeled with DAPI (blue) in the Cg (E), Pir (E), Ect (F), and Ent (F) of the tree shrew brain. For A–F, left-side coronal schematics show locations of stained sections; areas indicated with yellow or green dotted lines are magnified and shown in the right panels. A1–A4, B1–B4, C1–C4, and D1–D6 are magnified from the corresponding regions in the right panels of A, B, C, and D, respectively. Left panels of Figure 1B and 1C are taken from the same image. Left panels of Figure 1D and 1E are taken from the same image. Left panels of Figure 1F and 4F are taken from the same figure. Scale bars are shown in each image. AOB: Accessory olfactory bulb; AON: Anterior olfactory nucleus; AOD: Anterior olfactory nucleus, dorsal part; AOE: Anterior olfactory nucleus, external part; AOL: Anterior olfactory nucleus, lateral part; AOM: Anterior olfactory nucleus, medial part; AOP: Anterior olfactory nucleus, posterior part; AOV: Anterior olfactory nucleus, ventral part; Cg: Cingulate cortex; E: Ependyma and subependymal layer; Ect: Ectorhinal cortex; Ent: Entorhinal cortex; EPIA: External plexiform layer of the accessory olfactory bulb; EPI: External plexiform layer of the olfactory bulb; GlA: Glomerular layer of the accessory olfactory bulb; GL: Glomerular layer of the olfactory bulb; GCL: Granule cell layer; GrA: Granule cell layer of the accessory olfactory bulb; IPI: Internal plexiform layer of the olfactory bulb; MOB: Main olfactory bulb; MiA: Mitral cell layer of the accessory olfactory bulb; MCL: Mitral cell layer of the olfactory bulb; ONL: Olfactory nerve layer; Pir: Piriform cortex; WM: White matter.

medial septal nucleus (MS) and septohippocampal nucleus (SHi) (Figure 3F–H). In the lateral septal nucleus (LS), astrocyte density was low in the rostral and caudal portions but increased markedly in the middle subdivision (Figure 3F–H). Moderately dense populations were found in the nucleus of the horizontal limb of the diagonal band (HDB) (Figure 3I), nucleus of the vertical limb of the diagonal band (VDB; Figure 3I), and lateral preoptic area (LPO) (Figure 3J). GFAP-ir astrocytes were sparsely distributed in the bed nucleus of the stria terminalis (BST) (Figure 3J).

Diencephalon

Hypothalamus: In the supraoptic region, GFAP-ir astrocytes were abundantly distributed in the supraoptic nucleus (SON) and suprachiasmatic nucleus (SCN) (Figure 4A, B). Similarly, dense astrocytes were observed in nearly all subregions of the paraventricular nucleus (PVN), with clear somata and highly intertwined fibers lacking clear organization (Figure 4B). Notably, an exceptionally high density of astrocytes was concentrated around the periventricular region of the third ventricle (Figure 4B), with astrocytes also observed in the periventricular hypothalamic nucleus (Pe) (Figure 4B).

In the tuberal region, scattered GFAP-ir astrocytes were present in the dorsomedial hypothalamic nucleus (DMH) and ventromedial hypothalamic nucleus (VMH) (Figure 4C). The lateral hypothalamic area (LH) showed a moderate astrocyte density (Figure 4C), whereas the arcuate hypothalamic nucleus (Arc) exhibited a high density of GFAP-ir astrocytes (Figure 4D, E).

Within the mammillary region, which comprises the mammillary bodies and tuberomammillary nucleus, GFAP-ir astrocytes were moderately dense in both the lateral (SuML) and medial (SuMM) parts of the supramammillary nucleus (Figure 4D–F). A substantial number of astrocytes were also detected in the lateral mammillary nucleus (LM) (Figure 4D, E). In contrast, astrocyte density in the lateral part of the mammillary nucleus (ML) gradually decreased from rostral to caudal (Figure 4D–F). The medial part of the mammillary nucleus (MM) exhibited a moderate astrocyte density (Figure 4D, E).

Thalamus: Substantial densities of GFAP-ir astrocytes were observed in the anterior part of paraventricular thalamic nucleus (PVA), posterior part of paraventricular thalamic nucleus (PVP), rhomboid thalamic nucleus (Rh), medial habenular nucleus (MHb), lateral habenular nucleus (LHb), parafascicular thalamic nucleus (PF), and mediodorsal thalamic nucleus (MD) (Figure 4G–I). The nucleus of the stria medullaris (sm) also contained a large astrocyte population

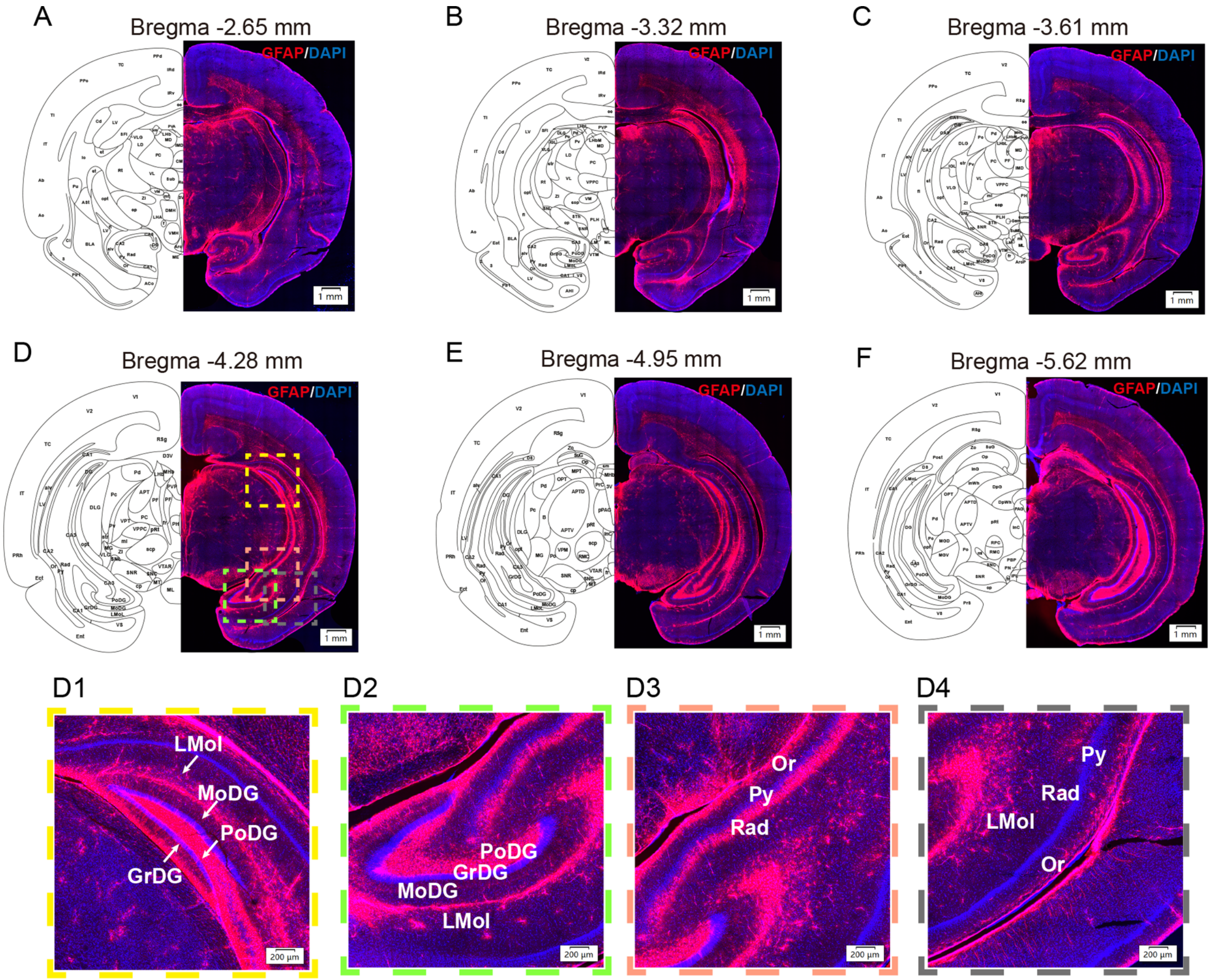

Figure 2 GFAP immunoreactivity in the hippocampus

A–F: Coronal sections from rostral to caudal showing GFAP immunoreactivity (red) co-labeled with DAPI (blue) in the hippocampus of the tree shrew brain. For A–F, left-coronal schematics show locations of stained sections. Areas indicated with colored dotted lines in D are magnified in D1–D4. Figure 2E and left panel of 4K are taken from the same image. Figure 2F and left panel of 4M are taken from the same image. Scale bars are shown in each image. GrDG: Granular cell layer; LMol: Lacunosum moleculare layer; MoDG: Molecular cell layer; Or: Oriens layer; PoDG: Polymorph cell layer; Py: Pyramidal cell layer; Rad: Radiatum layer.

(Figure 4G). In contrast, low densities of astrocytes were scattered throughout the paracentral thalamic nucleus (PC), anteroventral thalamic nucleus (AV), reuniens nucleus (Re), central medial thalamic nucleus (CM), and zona incerta of the thalamus (ZI) (Figure 4G–J). In the pretectal nucleus (PT), numerous GFAP-ir astrocytes were found in the medial pretectal nucleus (MPT) and olivary pretectal nucleus (OPT) (Figure 4K).

The geniculate nucleus includes the dorsal lateral geniculate nucleus (DLG), dorsal cap (DC), intergeniculate leaflet (IGL), ventral lateral geniculate nucleus (VLG), and medial geniculate nucleus (MG) (Figure 4L, M). Notably, GFAP-ir astrocytes were densely distributed in the DLG and VLG (Figure 4L), while sparsely to moderately distributed in the MG and IGL (Figure 4L, M).

Mesencephalon

The midbrain tectum is comprised of the superior colliculi (SC) and inferior colliculi (IC). GFAP-ir astrocytes were present across all subregions of the SC (Figure 5A). A particularly high density of astrocytes was observed in the zonal layer of the superior colliculus (Zo) (Figure 5A). Other SC layers, including the superficial gray (SuG), intermediate gray (InG), intermediate white (InWh), and deep gray colliculus (DpG), exhibited variable astrocyte densities ranging from sparse to dense (Figure 5A). The optic nerve layer (Op) contained sparse to moderate GFAP-ir astrocytes (Figure 5A), while the deep white layer (DpWh) showed sparse distribution (Figure 5A). In the IC, only a small number of GFAP-ir astrocytes were detected (Figure 5B).

Substantial GFAP-ir astrocyte populations were also observed in the substantia nigra (SN) and dorsal raphe nucleus (DR) (Figure 5C, D). In contrast, the parabrachial pigmented nucleus (PBP) of the ventral tegmental area (VTA) displayed sparse to moderate astrocyte densities (Figure 5C).

Additionally, a considerable number of GFAP-ir astrocytes were observed in the interpeduncular nucleus (IP), median raphe nucleus (MnR), retrorubral field (RRF), and periaqueductal gray (PAG) (Figure 5C, D).

Metencephalon and myelencephalon

High densities of GFAP-ir astrocytes were detected across

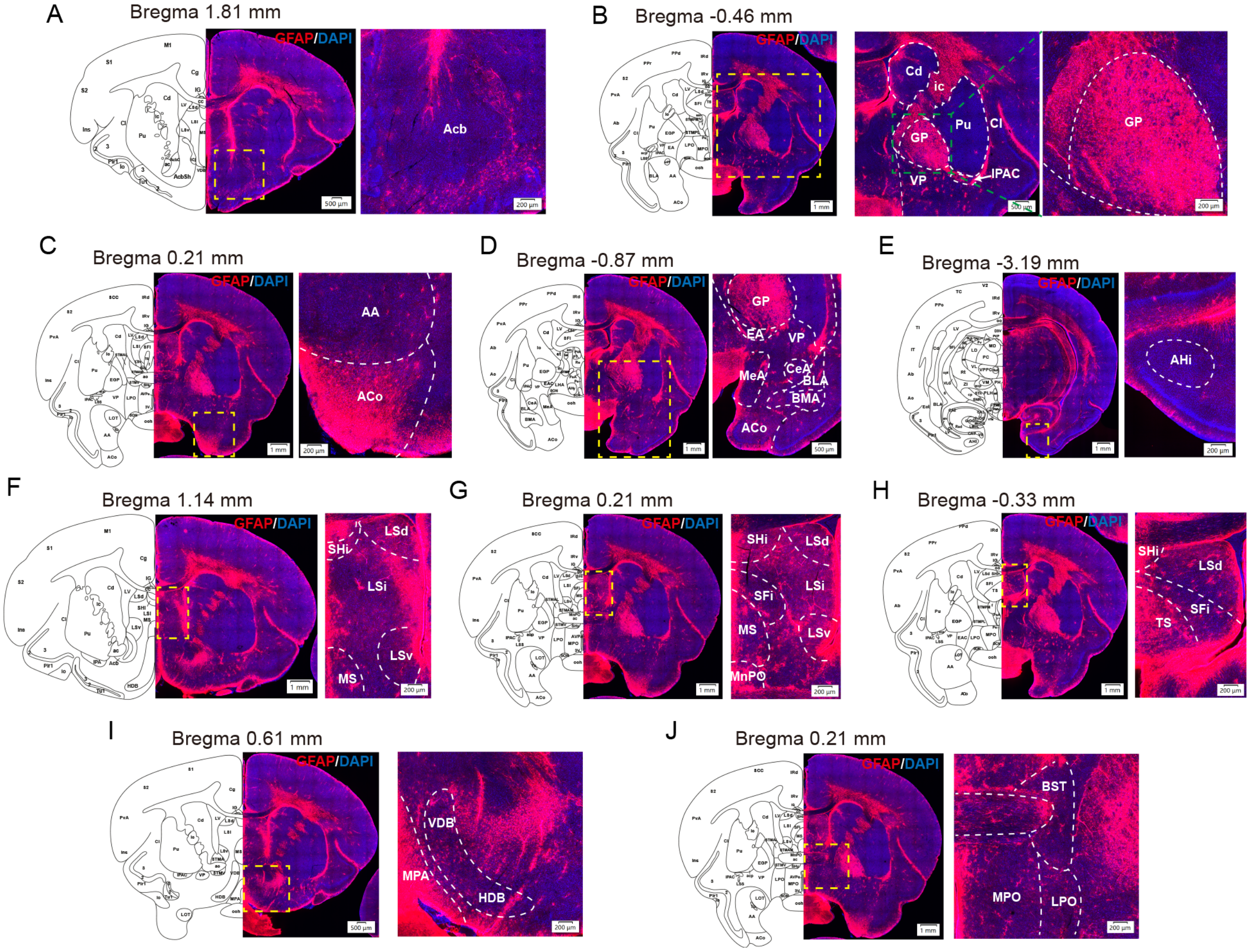

Figure 3 GFAP immunoreactivity in the basal ganglia, amygdala, septal, and preoptic regions

A, B: Representative images showing GFAP immunoreactivity (red) co-labeled with DAPI (blue) in the Acb, Cd, ic, Pu, GP, VP, Cl, and IPAC of the tree shrew brain. C–E: Coronal sections from rostral to caudal showing GFAP immunoreactivity (red) co-labeled with DAPI (blue) in the amygdala of the tree shrew brain. F–H: Coronal sections from rostral to caudal showing GFAP immunoreactivity (red) co-labeled with DAPI (blue) in the septal and preoptic areas of the tree shrew brain. I, J: Representative images showing GFAP immunoreactivity (red) co-labeled with DAPI (blue) in the VDB, HDB, MPA, LPO, MPO, and BST of the tree shrew brain. For A–J, left-coronal schematics show locations of stained sections. For A, C–J, areas indicated with yellow dotted lines are magnified and shown in the right panels. For B, area indicated with yellow dotted lines is magnified and shown in the middle panel; area indicated with green dotted lines in the middle panel is magnified and shown in the right panel. Left panels of Figure 3C, 3G, and 3J are taken from the same image. Scale bars are shown in each image. AA: Anterior amygdaloid area; Acb: Accumbens nucleus; Aco: Anterior cortical amygdaloid nucleus; AHi: Amygdalohippocampal area; BLA: Basolateral amygdaloid nucleus; BMA: Basomedial amygdaloid nucleus; BST: Bed nucleus of the stria terminalis; Cd: Caudate nucleus; CeA: Central amygdaloid nucleus; Cl: Claustrum; EA: Sublenticular extended amygdala; GP: Globus pallidus; HDB: Nucleus of the horizontal limb of the diagonal band; ic: Internal capsule; IPAC: Interstitial nucleus of the posterior limb of the anterior commissure; LPO: Lateral preoptic area; LSd: Lateral septal nucleus, dorsal part; LSi: Lateral septal nucleus, intermediate part; LSv: Lateral septal nucleus, ventral part; MeA: Medial amygdaloid nucleus; MnPO: Median preoptic nucleus; MPA: Medial preoptic area; MPO: Medial preoptic nucleus; MS: Medial septal nucleus; Pu: Putamen; SFi: Septofimbrial nucleus; SHi: Septohippocampal nucleus; TS: Triangular septal nucleus; VDB: Nucleus of the vertical limb of the diagonal band; VP: Ventral pallidum.

multiple regions of the metencephalon and myelencephalon, including the pontine nuclei (Pn), dorsal tegmental nucleus (DTg), laterodorsal tegmental nucleus (LDTg), locus coeruleus (LC), medial cerebellar nucleus (Med), facial nucleus (7N), intermediate reticular nucleus (IRt), gigantocellular reticular nucleus (Gi), and lateral cerebellar nucleus (Lat) (Figure 5C, E–G).

Astrocyte density and morphological characteristics in tree shrew and mouse brain

To examine interspecies differences in astrocyte density and morphology, 10 anatomically defined brain regions of interest were selected from tree shrews and mice.

Astrocytes in the hippocampus

In tree shrews, GFAP-ir astrocyte density gradually increased along the rostrocaudal axis within the CA1, CA3, and DG regions of the hippocampus (Figure 6A, C, E, G, I, K). In contrast, no significant rostrocaudal differences in astrocyte density were observed in the mouse hippocampus (Figure 6A, B, E, F, I, J). Quantitative comparisons revealed that astrocyte density in the tree shrew hippocampus was lower than that in mice (Figure 6D, H, L). Semi-automated quantitative morphometry based on 3D reconstruction was performed to investigate the morphological characteristics of GFAP-ir astrocytes in the CA1, CA3, and DG regions of both species (Figure 7A–F). In tree shrews, astrocytes located in the caudal

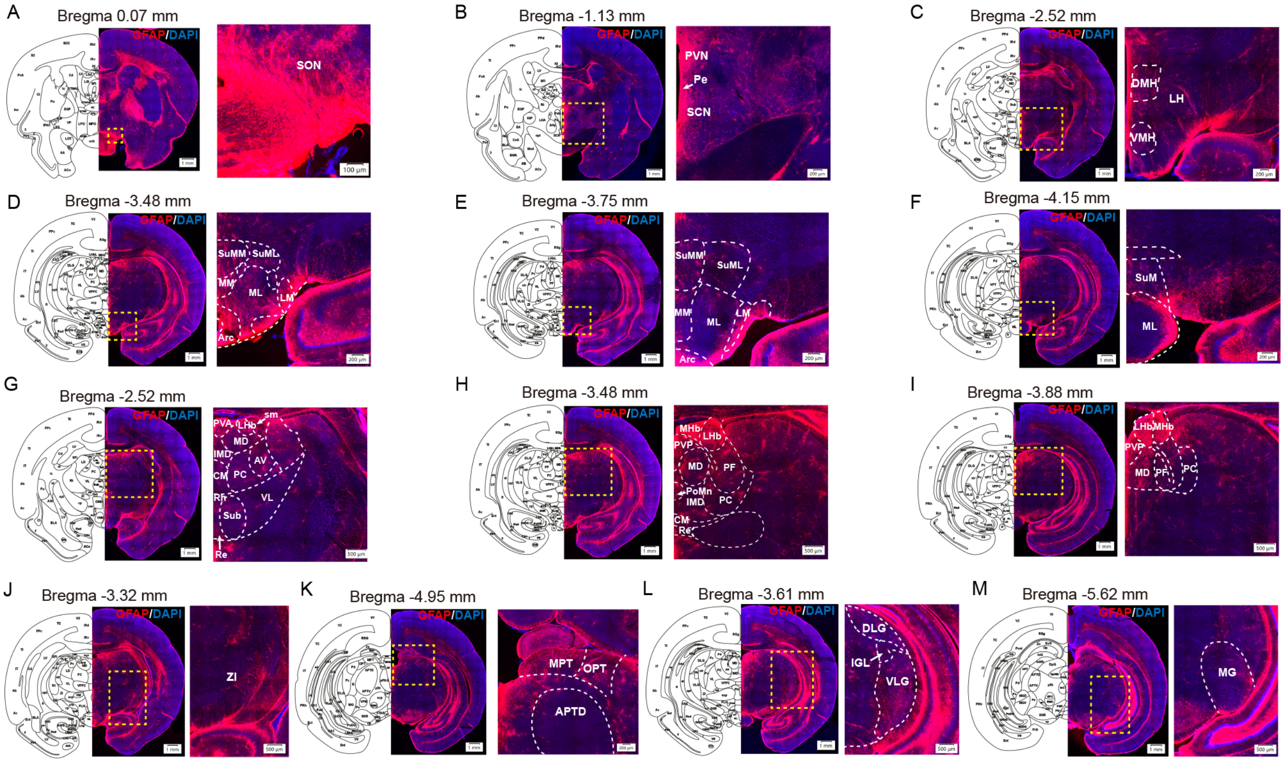

Figure 4 GFAP immunoreactivity in the hypothalamus and thalamus

A, B: Representative images showing GFAP immunoreactivity (red) co-labeled with DAPI (blue) in the SON, SCN, PVN, and Pe of the tree shrew brain. C: Representative image showing GFAP immunoreactivity (red) co-labeled with DAPI (blue) in the LH, DMH, and VMH of the tree shrew brain. D–F: Coronal sections showing GFAP immunoreactivity (red) co-labeled with DAPI (blue) from rostral to caudal in the mammillary nucleus of the tree shrew brain. G–I: Coronal sections from rostral to caudal showing GFAP immunoreactivity (red) co-labeled with DAPI (blue) in the habenular nucleus and thalamic nucleus of the tree shrew brain. J, K: Representative images showing GFAP immunoreactivity co-labeled with DAPI (blue) in the ZI, MPT, OPT, and APTD of the tree shrew brain. L, M: Representative images showing GFAP immunoreactivity (red) co-labeled with DAPI (blue) in the geniculate nucleus of the thalamus, including DLG, IGL, VLG, and MG, of the tree shrew brain. For A–M, left-coronal schematics show locations of stained sections; areas indicated with yellow dotted lines are magnified and shown in the right panels. Left panels of Figure 4D and 4H are taken from the same image. Left panels of Figure 4F and 1F are taken from the same image. Left panels of Figure 4K and 2E are taken from the same image. Left panels of Figure 4M and 2F are taken from the same image. Scale bars are shown in each image. APTD: Anterior pretectal nucleus, dorsal part; Arc: arcuate hypothalamic nucleus; AV: Anteroventral thalamic nucleus; CM: Central medial thalamic nucleus; DLG: Dorsal lateral geniculate nucleus; DMH: Dorsomedial hypothalamic nucleus; IGL: Intergeniculate leaflet; IMD: Intermediodorsal thalamic nucleus; LH: lateral hypothalamic area; LHb: Lateral habenular nucleus; LM: lateral mammillary nucleus; MD: Mediodorsal thalamic nucleus; MG: Medial geniculate nucleus; ML: Medial mammillary nucleus, lateral part; MHb: Medial habenular nucleus; MM: Medial mammillary nucleus, medial part; MPT: Medial pretectal nucleus; OPT: Olivary pretectal nucleus; PC: Paracentral thalamic nucleus; Pe: Periventricular hypothalamic nucleus; PF: Parafascicular thalamic nucleus; PoMn: Posteromedian thalamic nucleus; PVA: Paraventricular thalamic nucleus, anterior part; PVN: Paraventricular hypothalamic nucleus; PVP: Paraventricular thalamic nucleus, posterior part; Re: Reuniens thalamic nucleus; Rh: Rhomboid thalamic nucleus; SCN: Suprachiasmatic nucleus; sm: Stria medullaris of the thalamus; SN: Substantia nigra; SON: Supraoptic nucleus; SuM: Supramammillary nucleus; SuML: Supramammillary nucleus, lateral part; Sub: Submedius thalamic nucleus; SuMM: Supramammillary nucleus, medial part; VL: Ventrolateral thalamic nucleus; VLG: Ventral lateral geniculate nucleus; VMH: Ventromedial hypothalamic nucleus; ZI: Zona incerta.

hippocampus exhibited significantly longer and more elaborate filamentous processes compared to those in the rostral and middle regions (Figures 7A, C, E, 8A, C, E). No such regional differences in filament morphology were detected in mice (Figures 7B, D, F, 8A, C, E). In addition, tree shrew astrocytes in all three hippocampal subfields exhibited significantly longer and larger filament processes than those in mice (Figure 8A, C, E). Sholl analysis further demonstrated that astrocytes in the CA1, CA3, and DG regions of tree shrews displayed a higher number of radial intersections from the cell body compared to their murine counterparts (Figure 8B, D, F). Collectively, these results suggest that tree shrew hippocampal astrocytes exhibit lower cellular density but markedly greater structural complexity relative to those in mice.

Astrocytes in the hypothalamus

Astrocytes are enriched in the hypothalamus of rodents (Hajdarovic et al., 2022; Kálmán & Hajós, 1989). In the present study, astrocyte density and morphology were systematically examined in the hypothalamus of both tree shrews and mice. Within the PVN, astrocyte density peaked in the middle part in both species, with lower densities observed in the rostral and caudal parts (Supplementary Figure S8A–C). However, no significant interspecies differences in overall astrocyte density were detected in the PVN (Supplementary Figure S8D). Morphological analyses revealed that in the

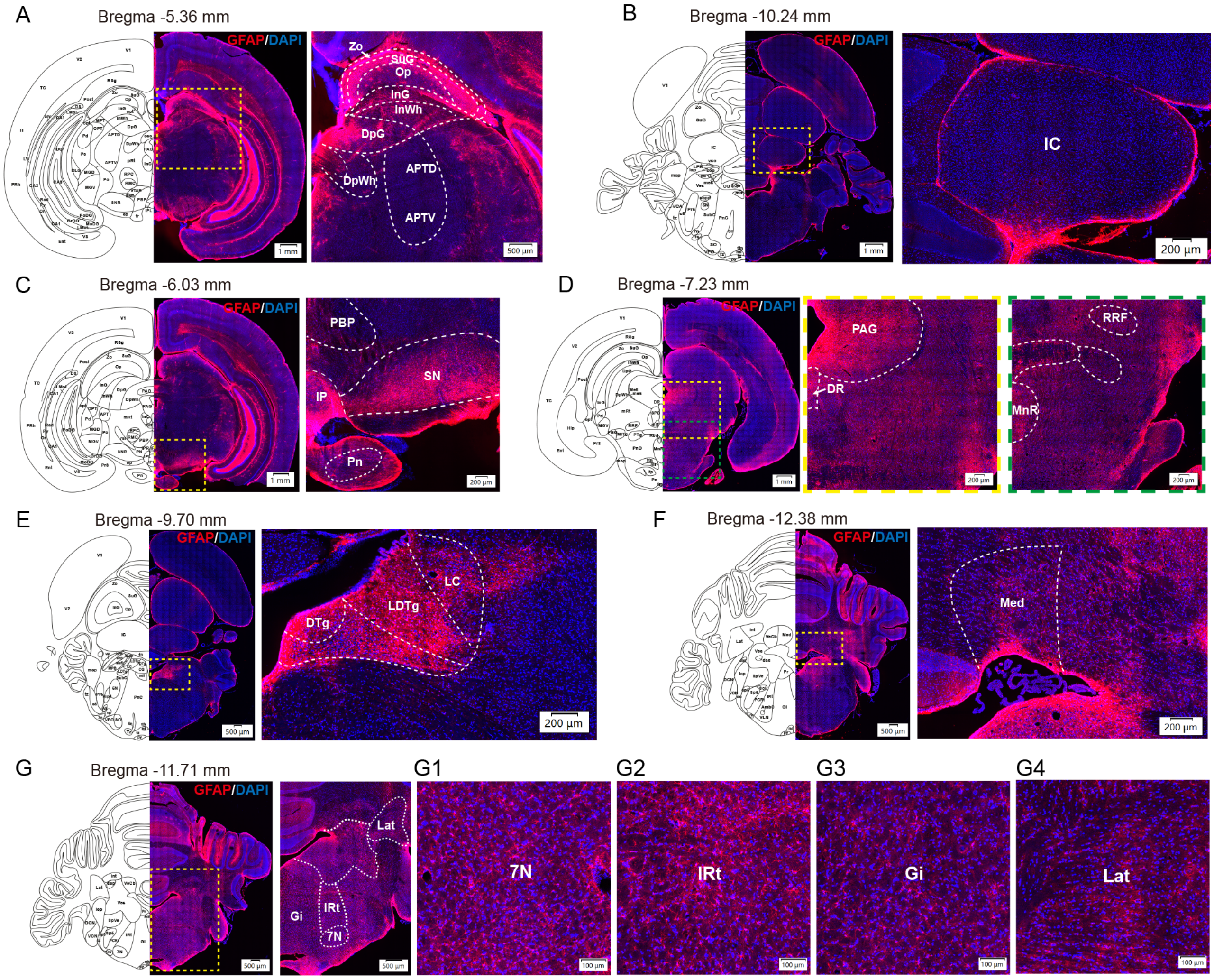

Figure 5 GFAP immunoreactivity in the mesencephalon and metencephalon/myelencephalon

A: Representative image showing GFAP immunoreactivity (red) co-labeled with DAPI (blue) in the superior colliculus and anterior pretectal nucleus of the tree shrew brain. B–D: Representative images showing GFAP immunoreactivity (red) co-labeled with DAPI (blue) in the IC, IP, Pn, SN, PBP, PAG, DR, RRF, and MnR of the tree shrew brain. E, F: Representative images showing GFAP immunoreactivity (red) co-labeled with DAPI (blue) in the LC, LDTg, DTg, and Med of the tree shrew brain. G: Representative image showing GFAP immunoreactivity (red) co-labeled with DAPI (blue) in the 7N, IRt, Gi, and Lat of the tree shrew brain. For A–G, left-coronal schematics show locations of stained sections; areas indicated with yellow or green dotted lines are magnified and shown in the right panels. G1–G4 are magnified from the corresponding regions shown in the right panel of G. Scale bars are shown in each image. 7N: Facial nucleus; APTD: Anterior pretectal nucleus, dorsal part; APTV: Anterior pretectal nucleus, ventral part; DpG: Deep gray layer of the superior colliculus; DpWh: Deep white layer of the superior colliculus; DR: Dorsal raphe nucleus; DTg: Dorsal tegmental nucleus; Gi: Gigantocellular reticular nucleus; IC: Inferior colliculus; InG: Intermediate gray layer of the superior colliculus; InWh: Intermediate white layer of the superior colliculus; IP: Interpeduncular nucleus; IRt: Intermediate reticular nucleus; Lat: Lateral cerebellar nucleus; LC: Locus coeruleus; LDTg: Laterodorsal tegmental nucleus; Med: Medial cerebellar nucleus; MnR: Median raphe nucleus; Op: Optic nerve layer of the superior colliculus; PAG: Periaqueductal gray; PBP: Parabrachial pigmented nucleus of the VTA; Pn: Pontine nuclei; RRF: Retrorubral field; SN: Substantia nigra; Zo: Zonal layer of the superior colliculus.

rostral PVN, tree shrew astrocytes exhibited shorter filament processes and fewer intersections than those in mice (Supplementary Figure S8E–I, J1). In contrast, astrocytes in the middle PVN of tree shrews had a significantly higher number of intersections relative to mice (Supplementary Figure S8J2), while no significant difference was observed in the caudal PVN (Supplementary Figure S8J3). These findings suggest that although astrocyte density in the PVN is similar between tree shrews and mice, branching complexity differs in a region-specific manner.

In the posterior hypothalamic nucleus (PH) and LH, a decreasing rostrocaudal gradient in astrocyte density was observed in both species (Supplementary Figures S9A–C, S10A–C). Notably, astrocyte density in the PH was significantly higher in tree shrews than mice, a difference not observed in the LH (Supplementary Figures S9D, S10D). In the PH, tree shrew astrocytes exhibited longer and larger filament processes and a greater number of intersections compared to mice (Supplementary Figure S9E–I, J1–3). In the LH, increased filament length and intersection count in tree shrew astrocytes were observed specifically in the caudal subdivision (Supplementary Figure S10E–I, J1–3). These results suggest that astrocytes in the PH, but not the LH, exhibited both higher density and greater morphological complexity in tree shrews than in mice.

In the DMH, astrocyte density declined rostrocaudally in

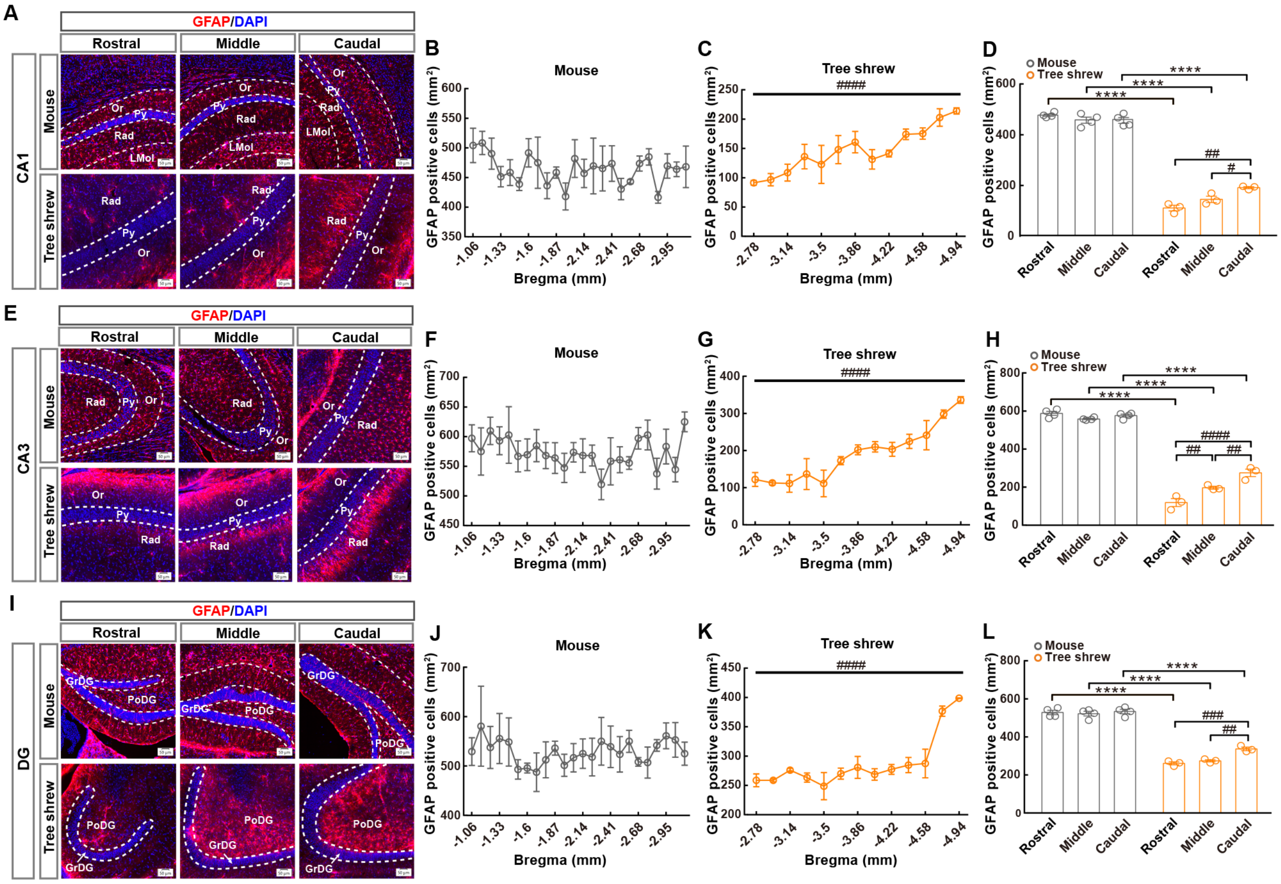

Figure 6 Distribution patterns of GFAP-ir astrocytes in the hippocampus of tree shrews and mice

A, E, I: Representative images showing GFAP immunoreactivity (red) co-labeled with DAPI (blue) from rostral to caudal in the CA1 (A), CA3 (E), and DG (I) of the mouse (upper panels) and tree shrew brains (lower panels). B, C, F, G, J, K: Densities of GFAP-ir cells from rostral to caudal in the CA1 (B, C), CA3 (F, G), and DG (J, K) of the mouse and tree shrew brains. D, H, L: Quantification of GFAP-ir astrocyte densities from rostral to caudal in the CA1 (D), CA3 (H), and DG (L) of mouse and tree shrew brains. Data are shown as the mean±SEM. For B, C, F, G, J, and K, one-way repeated-measures ANOVA, main effect of location relative to bregma, $^{\#\#\#\#}$: $P<0.0001$; for D, H, and L, two-way repeated-measures ANOVA, Bonferroni *post hoc* test, ****: $P<0.0001$, $^{\#}$: $P<0.05$, $^{\#\#}$: $P<0.01$, $^{\#\#\#}$: $P<0.001$, $^{\#\#\#\#}$: $P<0.0001$; $n=4$ mice and 3 tree shrews. Scale bars: 50 μm. For detailed statistics, see Supplementary Table S2. GrDG: Granular cell layer; LMol: Lacunosum moleculare layer; Or: Oriens layer; PoDG: Polymorph cell layer; Py: Pyramidal cell layer; Rad: Radiatum layer.

mice but remained relatively stable in tree shrews (Supplementary Figure S11A–C). Conversely, in the VMH, tree shrews rather than mice exhibited a significant rostrocaudal decrease in astrocyte density (Supplementary Figure S12A–C). Further analyses revealed higher astrocyte densities in both the DMH and VMH of tree shrews relative to mice (Supplementary Figure S11D, Supplementary Figure S12D). Furthermore, astrocytes in these regions exhibited longer filament processes and a higher number of intersections in tree shrews compared to mice (Supplementary Figures S11E–I, J1–3, S12E–I, J1–3). Collectively, these results demonstrate that in the DMH and VMH, tree shrew astrocytes exhibit both higher density and enhanced morphological complexity compared to those in mice.

Astrocytes in the substantia nigra and periaqueductal gray

In the SN of tree shrews, astrocyte density showed a gradual rostrocaudal decline, a pattern not observed in mice (Supplementary Figure S13A–C). Specifically, astrocyte density in the caudal SN was markedly lower in tree shrews compared to mice (Supplementary Figure S13D). Astrocytes in the SN of tree shrews had longer and larger filament processes as well as a higher number of intersections compared to mice (Supplementary Figure S13E–I, J1–3). These findings suggest that in the SN, tree shrew astrocytes display reduced density caudally but greater morphological complexity along the rostrocaudal axis relative to mouse astrocytes.

In the PAG, a rostrocaudal increase in astrocyte density was observed in mice, whereas no such trend was evident in tree shrews (Supplementary Figure S14A–C). Overall, astrocyte density in the PAG was significantly higher in tree shrews than in mice (Supplementary Figure S14D). Tree shrew astrocytes in this region also exhibited longer and larger filament processes and a higher number of intersections compared to their murine counterparts (Supplementary Figure S14E–I, J1–3). These results suggest that astrocytes in the PAG of tree shrews demonstrate both higher density and greater morphological complexity compared to those in mice.

DISCUSSION

This study presents a comprehensive brain-wide mapping of GFAP-ir astrocytes in the tree shrew, revealing their distributional architecture across all major neuroanatomical

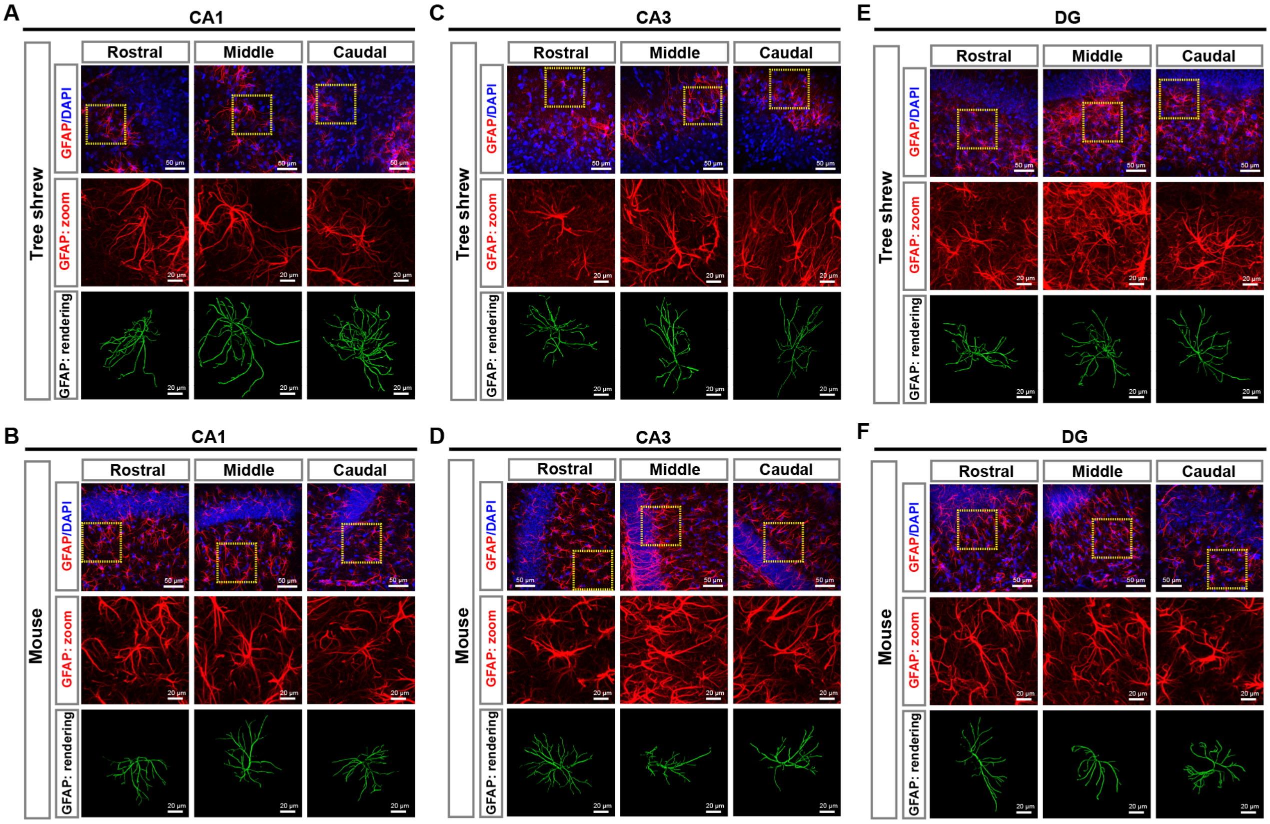

Figure 7 Representative images showing GFAP-ir astrocyte morphology in the hippocampus of tree shrews and mice

A, B: Representative images of GFAP immunofluorescence (red) and three-dimensional (3D) reconstruction (green) of astrocytes from rostral to caudal in the hippocampal CA1 region in tree shrew (A) and mouse brains (B). C, D: Representative images of GFAP immunofluorescence (red) and 3D reconstruction (green) of astrocytes from rostral to caudal in the hippocampal CA3 region in tree shrew (C) and mouse brains (D). E, F: Representative images of GFAP immunofluorescence (red) and 3D reconstruction (green) of astrocytes from rostral to caudal in the hippocampal DG region in tree shrew (E) and mouse brains (F). Areas indicated with yellow dotted lines are magnified and shown in the “GFAP: zoom” images. Scale bars: 50 μm (overview) and 20 μm (zoom and rendering).

divisions. High astrocytic densities were observed in the E, GL, GlA, GrA, layer I of the cerebral cortex, PoDG, GP, MPA, MnPO, TS, OPT, PVP, LHb, MHb, IP, SN, Zo, DTg, Gi, IRt, Lat, LDTg, Med, lateral parabrachial nucleus (LPB), and hypothalamus. The global distributional profile of GFAP-ir astrocytes in the tree shrew showed striking similarities with previously characterized astrocytic patterns in the rat brain (Hajós & Kálmán, 1989; Kálmán & Hajós, 1989), suggesting conserved organizational principles across species. Beyond mapping, this investigation provides a systematic interspecies comparison of GFAP-ir astrocyte density spanning the telencephalic, diencephalic, mesencephalic, metencephalic, and myelencephalic regions, revealing region-specific divergence between tree shrews and mice. Notably, this research delivers the first detailed quantitative assessment of astrocytic density and morphology in critical neurofunctional structures, including the CA1, CA3, DG, PVN, PH, LH, DMH, VMH, SN, and PAG, across both species.

These findings yield several important implications. First, the detailed anatomical and morphological atlas of astrocytes in the tree shrew offers a foundational reference for delineating more precise brain region boundaries and enables region-specific functional analyses of astrocyte roles. Second, the systematic distributional data advance our understanding of glial evolutionary trajectories, bridging the phylogenetic gap between rodents and primates and providing insight into astrocyte diversification in the primate lineage. Finally, cross-species analysis of astrocytic architecture and expression patterns highlights both conserved and divergent features of astrocyte organization, which may shed light on the shared pathophysiological mechanisms underlying neuropsychiatric disorders.

Species comparisons of GFAP-ir astrocyte distribution and functional relevance Telencephalon

The MOB is divided into seven distinct layers, ranging from the superficial to deep, including the ONL, GL, EPl, MCL, IPl, GCL, and subependymal zone (SZ) (Bailey & Shipley, 1993). In tree shrews, GFAP-ir astrocytes exhibited a pronounced laminar distribution, with particularly high densities in the E, GL, ONL, and GlA, closely mirroring the distribution observed in mice. However, interspecies differences emerged in the IPl and MCL regions, where astrocytic fibers in tree shrews appeared sparse or limited, contrasting with the dense distribution seen in mice. Such divergences suggest species-specific modulation of glial architecture in olfactory processing regions. Comparative data from rats and humans further underscore the variability in astrocyte distribution (Bailey & Shipley, 1993; Rahimian et al., 2024). In rats, robust GFAP expression is observed in the GL and SZ, with moderate immunoreactivity in the EPl and reduced labeling in the GCL (Bailey & Shipley, 1993). In humans, GFAP-ir astrocyte density is high in the ON and GL but low in the EPl and MCL, with astrocytes in the SZ of the olfactory bulb exhibiting extremely high density (Chiu & Greer, 1996). These variations

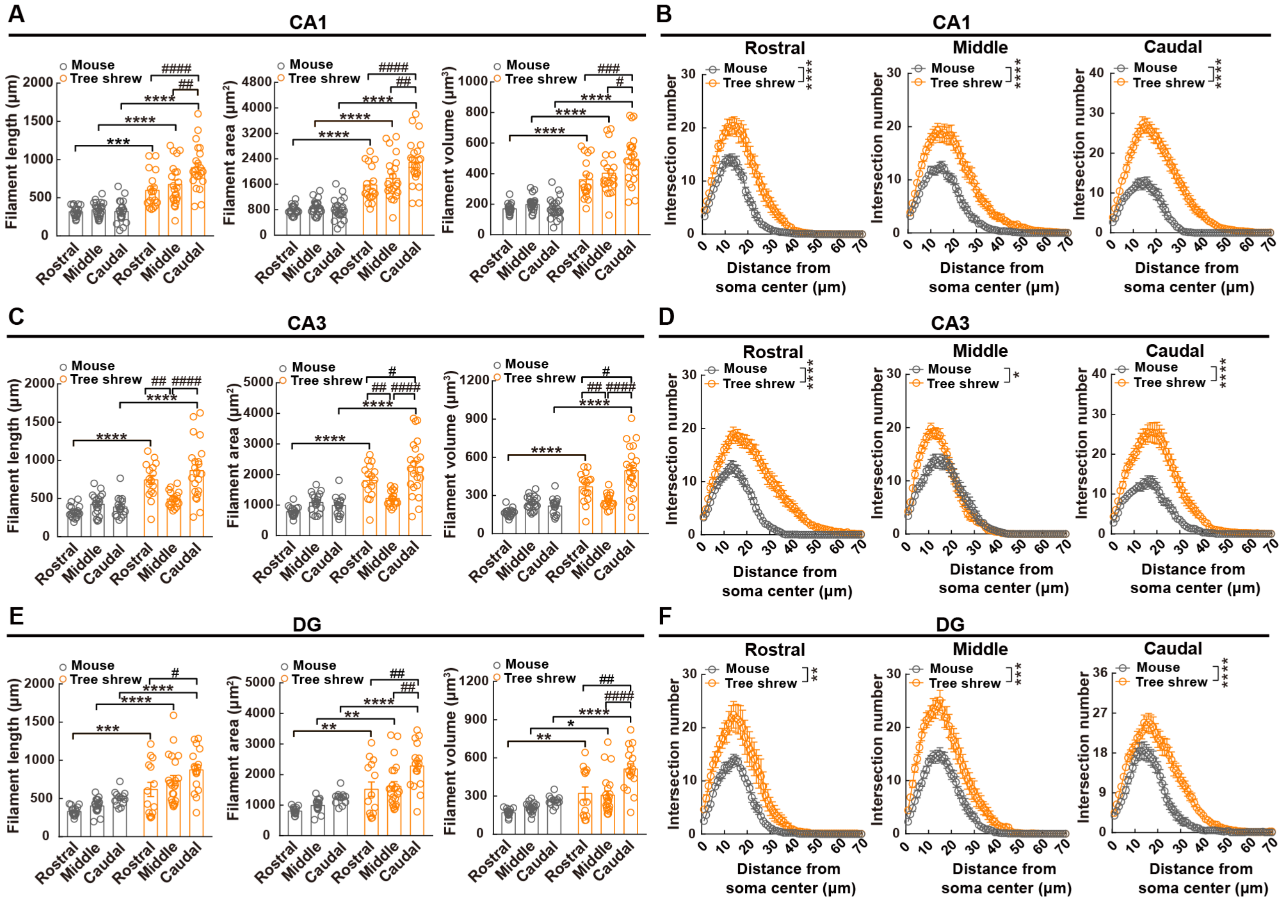

Figure 8 Quantifications and Sholl analyses of GFAP-ir astrocytic processes in the hippocampus of tree shrews and mice

A, C, E: Imaris-based automated quantification of GFAP-ir astrocytic filament length, filament area, and filament volume from rostral to caudal in the CA1 (A), CA3 (C), and DG (E) of mouse and tree shrew brains. B, D, F: Sholl analyses of astrocytic morphology from rostral to caudal in the CA1 (B), CA3 (D), and DG (F) of mouse and tree shrew brains. Data are shown as the mean±SEM. For A, C, and E, two-way ANOVA, Bonferroni *post hoc* test, *: $P<0.05$, **: $P<0.01$, ***: $P<0.001$, ****: $P<0.0001$, $^{\#}$: $P<0.05$, $^{\#\#}$: $P<0.01$, $^{\#\#\#}$: $P<0.001$, $^{\#\#\#\#}$: $P<0.0001$; for B, D, and F, two-way repeated-measures ANOVA, main effect of species, *: $P<0.05$, **: $P<0.01$, ***: $P<0.001$, ****: $P<0.0001$. CA1-mouse (rostral: $n=19$ cells; middle: $n=23$ cells; caudal: $n=22$ cells); CA1-tree shrew (rostral: $n=18$ cells; middle: $n=22$ cells; caudal: $n=22$ cells). CA3-mouse (rostral: $n=18$ cells; middle: $n=20$ cells; caudal: $n=17$ cells); CA3-tree shrew (rostral: $n=16$ cells; middle: $n=16$ cells; caudal: $n=22$ cells). DG-mouse (rostral: $n=17$ cells; middle: $n=18$ cells; caudal: $n=13$ cells); DG-tree shrew (rostral: $n=14$ cells; middle: $n=22$ cells; caudal: $n=17$ cells). For detailed statistics, see Supplementary Table S2.

point to conserved yet flexible glial adaptations that likely support species-specific demands in olfactory signal integration. Notably, astrocytes have been implicated in modulating olfactory bulb circuits, and disruptions in astrocytic function have been linked to impaired sensory processing (Sardar et al., 2023; Ung et al., 2020, 2021).

Cortical structures are generally delineated as six layers of neurons that emerge in a sequential manner during the early stages of development (Eiraku et al., 2008). These structures play a critical role in motor, sensory, and cognitive functions (Bayraktar et al., 2020). In the tree shrew, GFAP-ir astrocytes were enriched in layer I and predominantly localized to the perivascular area, while layers II–VI showed sparse immunoreactivity. In contrast, mice exhibited weak GFAP immunoreactivity in layer I and virtually no detectable labeling in layers II–VI. Interestingly, GFAP-ir astrocytes were occasionally prominent in the Pir1 and Ent of mice, a pattern not observed in tree shrews. These findings may reflect species-specific differences in astrocytic maturation and regional specialization. During cortical development, GFAP-ir astrocyte distribution varies dynamically across regions and laminae (Amenta et al., 1998; Hodge et al., 2019), and mature astrocyte subtypes display functional and morphological profiles that differ between humans and rodents. Notably, primate-specific interlaminar astrocytes are located in layer I and extend long processes, whereas protoplasmic astrocytes populate layers II–VI.

In the hippocampal formation of the tree shrew, the rostral part first appeared in the ventral portion of the brain, consistent with previous anatomical observations in tree shrews and nonhuman primates (Keuker et al., 2003; Schwerdtfeger, 1984). GFAP-ir astrocytes were densely distributed in the CA1, CA3, and DG regions, excluding the granule and pyramidal cell layers, mirroring the general distribution observed in the mouse hippocampus. However, notable interspecies differences were also evident. In the tree shrew, astrocytic density in the hippocampus progressively increased along the rostrocaudal axis, a pattern not observed in mice. Comparative studies in other mammals have reported similar and divergent patterns. In adult dogs, GFAP-ir astrocytes are observed in all layers of the DG, with somata enriched in the polymorphic layer, and are primarily detected in the stratum oriens and radiatum, with sparse labeling in or near the pyramidal layer (Hwang et al., 2008). In adult rats, as in mice, astrocytic GFAP expression delineates the hippocampal cytoarchitecture, with morphology varying across layers (Kálmán & Hajós, 1989). A key finding of the present study was that tree shrew hippocampal astrocytes displayed lower overall density yet greater morphological complexity than those in mice. Given the essential role of the hippocampus in learning, memory formation and consolidation, and emotional regulation, including responses to fear, anxiety, and stress (Bartsch & Wulff, 2015), these morphological features may have important implications. Chronic stress has been shown to reduce hippocampal astrocyte density and induce structural atrophy in rodents (Murphy-Royal et al., 2019), with similar reductions in hippocampal astrocytes documented in individuals with major depressive disorder (Cobb et al., 2016; Rajkowska & Stockmeier, 2013). Tree shrews are highly sensitive to stress (Fang et al., 2016; Meng et al., 2016; Wang et al., 2011), and the reduced astrocyte density in their hippocampus may constitute a structural determinant linking astrocyte plasticity to stress vulnerability. Peripheral processes of astrocytes lie in close proximity to neuronal synapses, allowing them to modulate synaptic activity and contribute to the regulation of neural circuits (Allen, 2014; Cheng et al., 2023; Khakh & Deneen, 2019). Enhanced branching complexity has been proposed to promote physical interactions within the structural domains of astrocytes (Delgado-García et al., 2024). These processes have also been implicated in orchestrating neurotransmitter diffusion within the extracellular space (Lawal et al., 2022). By ensheathing synapses, astrocyte processes can limit glutamate spillover and prevent nonspecific trans-synaptic activation, thereby facilitating long-term potentiation and contributing to memory formation (Henneberger et al., 2020; Herde et al., 2020; Ota et al., 2013; Ventura & Harris, 1999). The high morphological complexity of hippocampal astrocytes in tree shrews may reflect an enhanced capacity for synaptic modulation and structural plasticity, potentially supporting learning-associated neural remodeling. These species-specific astrocytic features may underlie functional differences in hippocampal-dependent learning and memory between tree shrews and mice, offering a valuable framework for future comparative neurobiological investigations.

Our results indicated that astrocytes were sparsely distributed in the striatum (caudate-putamen), whereas the globus pallidus contained a markedly higher astrocytic density, consistent with prior observations in the rat brain (Kálmán & Hajós, 1989). Notably, the VP exhibited low GFAP immunoreactivity in tree shrews but showed relatively dense labeling in mice. GFAP-ir astrocytes were absent from the nucleus accumbens in mice but demonstrated sparse to moderate densities in tree shrews. In contrast, astrocytes exhibit enrichment in the marginal region of the nucleus accumbens in rats (Kálmán & Hajós, 1989).

In the tree shrew amygdala, GFAP-ir astrocytes exhibited sparse to moderate densities across most subregions, with no detectable labeling in the AHi. In contrast, dense GFAP-ir astrocytes were present in the AHi and EA of mice, with sparse distribution in other subregions of the amygdala. Across the septal and preoptic regions, astrocytic distribution patterns were broadly conserved between the two species.

Diencephalon

Astrocytes exhibit substantial evolutionary divergence across mammalian lineages, with notable increases in size and morphological complexity observed in primates compared with rodents (Ciuba et al., 2025). In the present study, astrocytes in the hypothalamus of tree shrews exhibited consistently higher densities and greater structural complexity compared to those in mice, aligning with the phylogenetic proximity of tree shrews to primates (Xiao et al., 2017). As a central regulator of autonomic, endocrine, and behavioral functions, the hypothalamus integrates diverse physiological inputs to maintain systemic homeostasis (Camandola, 2018). Astrocytes within the hypothalamic preoptic integrate nociception and thermoregulation (Jia et al., 2024), while those in the VMH and Arc sense hormonal and nutrient cues and regulate metabolism and energy homeostasis (Ameroso et al., 2022; García-Cáceres et al., 2019; Harrison et al., 2019). Tree shrews display elevated metabolic activity, with higher locomotor activity, heart rate, and core body temperature relative to rodents (Wang et al., 2013). The increased density and morphological complexity of hypothalamic astrocytes in tree shrews may reflect adaptations to these heightened physiological demands, potentially contributing to their unique characteristics. In the PVN, astrocyte densities were comparable between tree shrews and mice; however, the branching architecture varied depending on anatomical location, suggesting conserved astrocytic presence accompanied by region-specific structural divergence. Comparative analyses of PVN cytoarchitecture—including astrocytic organization —across primates, tree shrews, and rodents are needed in future research. In rodents, PVN astrocytes contribute to systemic glucose metabolism and adaptive responses to metabolic signals (Herrera Moro Chao et al., 2022). Obesity triggers anatomically restricted remodeling of astrocytic Ca^{2+} signaling in the PVN, and chemogenetic manipulation of these astrocytes exerts bidirectional control over systemic glucose metabolism and energy homeostasis (Herrera Moro Chao et al., 2022). Notably, tree shrews are more sensitive to glucose than rodents, positioning them as valuable translational models for investigating the astrocytic mechanisms underlying type 2 diabetes (Zhao et al., 2018). The distribution pattern of PVN astrocytes in tree shrews provides an anatomical basis for understanding the role of astrocytes in nutritional and metabolic diseases across mammalian species.

The thalamus, widely considered as the gateway to consciousness, plays a pivotal role in transmitting sensory and motor signals to the neocortex and in regulating sleep-related rhythms (Philippot et al., 2021). Structural remodeling of thalamic astrocytes has been linked to changes in attention and cognitive processing (Cho et al., 2022; Copeland et al., 2017). In the present analysis, the overall distribution patterns of GFAP-ir astrocytes across most thalamic regions were comparable between tree shrews and mice. However, markedly higher astrocytic densities were detected in tree shrews within specific thalamic nuclei, including the intermediodorsal thalamic nucleus (IMD), MD, DLG, PT, PVA and PVP, indicating region-specific amplification of astrocytic presence in the tree shrew thalamus.

Mesencephalon, metencephalon, and myelencephalon

In the tree shrew mesencephalon, GFAP-ir astrocytes were prominently distributed within the SC, DR, IP, MnR, PAG, RRF, SN, and ventral tegmental nucleus (VTg). Within the metencephalon and myelencephalon, dense astrocytic labeling was observed in the DTg, Gi, IRt, Lat, LPB, LDTg, LC, Med, and Pn. Across numerous brainstem regions, astrocyte densities in the tree shrew exceeded those measured in mice, indicating species-specific amplification of astrocytic representation. A detailed analysis of the SN revealed a rostrocaudal gradient in the tree shrew, characterized by declining astrocyte density toward the caudal pole accompanied by increasing morphological complexity —an organizational feature not observed in mice. These interspecies differences in astrocytic density and morphology may reflect differences in physiological and behavioral functions mediated by specific brain regions.

The functional role of astrocytes in the tree shrew SN remains largely uncharacterized. In mice, astrocytes located in the substantia nigra pars compacta (SNpc) have been shown to undergo age-associated increases in morphological complexity without corresponding increases in GFAP expression (Bondi et al., 2023). In contrast, studies in the human brain have reported age-related elevations in GFAP levels within the SN (Venkateshappa et al., 2012), suggesting that species-specific regulatory mechanisms may shape astrocytic dynamics in this region.

Limitations

This study has several limitations that should be mentioned. First, the limited sample size may constrain the statistical power of our conclusions, highlighting the need for larger cohorts in future comparative investigations. Furthermore, it is well established that a considerable proportion of astrocytes are GFAP-negative (Walz, 2000; Walz & Lang, 1998). As such, it is possible that the GFAP-ir population examined here may represent only a subset of the total astrocyte population. Further studies using alternative astrocytic markers, such as aldehyde dehydrogenase 1 family member L1 (ALDH1L1), are needed. Additionally, multiple astrocyte subtypes with distinct morphological profiles have been described in humans and rodents (Falcone & Martínez-Cerdeño, 2023; Schitine et al., 2015; Vasile et al., 2017), yet the morphological heterogeneity of astrocytes in the tree shrew brain remains uncharacterized, warranting future investigation.

CONCLUSION

The present study provides the first systematic, brain-wide atlas of GFAP-ir astrocyte distribution and morphology in tree shrews. The data provide an anatomical and morphological framework that may support future investigations into region-specific astrocyte function and their involvement in neurophysiological and behavioral processes.

SUPPLEMENTARY DATA

Supplementary data to this article can be found online.

COMPETING INTERESTS

The authors declare that they have no competing interests.

AUTHORS' CONTRIBUTIONS

P.C. and J.N.Z. conceived the study and revised the manuscript. Y.T.W. and Q.Q.X. performed most of the experiments and data analysis and drafted the manuscript. S.W.W., J.K.G., and S.D.W. contributed to morphological reconstruction. X.Y.Q., Q.H.S., and Y.W. provided helpful suggestions on methodology. R.Y.L. provided the reagents. Y.X.Y. and C.W.W. participated in the collection of animal samples. All authors read and approved the final version of the manuscript.

ACKNOWLEDGMENTS

We are grateful to colleagues from the Institute of Brain Science, The First Affiliated Hospital of Anhui Medical University for their advice and support during the project.

REFERENCES

Abbott NJ, Rönnbäck L, Hansson E. 2006. Astrocyte-endothelial interactions at the blood-brain barrier. *Nature Reviews Neuroscience*, **7**(1): 41–53.

Allen NJ. 2014. Astrocyte regulation of synaptic behavior. *Annual Review of Cell and Developmental Biology*, **30**: 439–463.

Amenta F, Bronzetti E, Sabbatini M, et al. 1998. Astrocyte changes in aging cerebral cortex and hippocampus: a quantitative immunohistochemical study. *Microscopy Research and Technique*, **43**(1): 29–33.

Ameroso D, Meng A, Chen S, et al. 2022. Astrocytic BDNF signaling within the ventromedial hypothalamus regulates energy homeostasis. *Nature Metabolism*, **4**(5): 627–643.

Andersen JV, Schousboe A, Verkhratsky A. 2022. Astrocyte energy and neurotransmitter metabolism in Alzheimer's disease: integration of the glutamate/GABA-glutamine cycle. *Progress in Neurobiology*, **217**: 102331.

Bailey MS, Shipley MT. 1993. Astrocyte subtypes in the rat olfactory bulb: morphological heterogeneity and differential laminar distribution. *Journal of Comparative Neurology*, **328**(4): 501–526.

Baldwin KT, Murai KK, Khakh BS. 2024. Astrocyte morphology. *Trends in Cell Biology*, **34**(7): 547–565.

Bartsch T, Wulff P. 2015. The hippocampus in aging and disease: from plasticity to vulnerability. *Neuroscience*, **309**: 1–16.

Bayraktar OA, Bartels T, Holmqvist S, et al. 2020. Astrocyte layers in the mammalian cerebral cortex revealed by a single-cell in situ transcriptomic map. *Nature Neuroscience*, **23**(4): 500–509.

Bondi H, Chiazza F, Masante I, et al. 2023. Heterogenous response to aging of astrocytes in murine *Substantia Nigra pars compacta* and *Pars reticulata*. *Neurobiology of Aging*, **123**: 23–34.

Cahill MK, Collard M, Tse V, et al. 2024. Network-level encoding of local neurotransmitters in cortical astrocytes. *Nature*, **629**(8010): 146–153.

Camandola S. 2018. Astrocytes, emerging stars of energy homeostasis. *Cell Stress*, **2**(10): 246–252.

Cheng YT, Luna-Figueroa E, Woo J, et al. 2023. Inhibitory input directs astrocyte morphogenesis through glial GABA$_B$R. *Nature*, **617**(7960): 369–376.

Chiu K, Greer CA. 1996. Immunocytochemical analyses of astrocyte development in the olfactory bulb. *Developmental Brain Research*, **95**(1): 28–37.

Cho FS, Vainchtein ID, Voskobiynyk Y, et al. 2022. Enhancing GAT-3 in thalamic astrocytes promotes resilience to brain injury in rodents. *Science Translational Medicine*, **14**(652): eabj4310.

Ciuba K, Piotrowska A, Chaudhury D, et al. 2025. Molecular signature of primate astrocytes reveals pathways and regulatory changes contributing to human brain evolution. *Cell Stem Cell*, **32**(3): 426–444. e14.

Cobb JA, O'neill K, Milner J, et al. 2016. Density of GFAP-immunoreactive astrocytes is decreased in left hippocampi in major depressive disorder. *Neuroscience*, **316**: 209–220.

Colombo JA, Fuchs E, Härtig W, et al. 2000. "Rodent-like" and "primate-like" types of astroglial architecture in the adult cerebral cortex of mammals: a comparative study. *Anatomy and Embryology*, **201**(2): 111–120.

Copeland CS, Wall TM, Sims RE, et al. 2017. Astrocytes modulate thalamic sensory processing via mGlu2 receptor activation. *Neuropharmacology*, **121**: 100–110.

Czéh B, Simon M, Schmelting B, et al. 2006. Astroglial plasticity in the hippocampus is affected by chronic psychosocial stress and concomitant fluoxetine treatment. *Neuropsychopharmacology*, **31**(8): 1616–1626.

Delgado-García LM, Ojalvo-Sanz AC, Nakamura TKE, et al. 2024. Dissecting reactive astrocyte responses: lineage tracing and morphology-based clustering. *Biological Research*, **57**(1): 54.

Duan Y, Jin LT, Du WJ, et al. 2022. Alterations of dopamine receptors and the adaptive changes of L-type calcium channel subtypes regulate cocaineseeking habit in tree shrew. *Life*, **12**(7): 984.

Eiraku M, Watanabe K, Matsuo-Takasaki M, et al. 2008. Self-organized formation of polarized cortical tissues from ESCs and its active manipulation by extrinsic signals. *Cell Stem Cell*, **3**(5): 519–532.

Endo F, Kasai A, Soto JS, et al. 2022. Molecular basis of astrocyte diversity and morphology across the CNS in health and disease. *Science*, **378**(6619): eadc9020.

Falcone C. 2022. Evolution of astrocytes: from invertebrates to vertebrates. *Frontiers in Cell and Developmental Biology*, **10**: 931311.

Falcone C, Martínez-Cerdeño V. 2023. Astrocyte evolution and human specificity. *Neural Regeneration Research*, **18**(1): 131–132.

Falcone C, Wolf-Ochoa M, Amina S, et al. 2019. Cortical interlaminar astrocytes across the therian mammal radiation. *Journal of Comparative Neurology*, **527**(10): 1654–1674.

Fang H, Sun YJ, Lv YH, et al. 2016. High activity of the stress promoter contributes to susceptibility to stress in the tree shrew. *Scientific Reports*, **6**: 24905.

Freeman MR. 2010. Specification and morphogenesis of astrocytes. *Science*, **330**(6005): 774–778.

Fuchs E. 2005. Social stress in tree shrews as an animal model of depression: an example of a behavioral model of a CNS disorder. *CNS Spectrums*, **10**(3): 182–190.

García-Cáceres C, Balland E, Prevot V, et al. 2019. Role of astrocytes, microglia, and tanycytes in brain control of systemic metabolism. *Nature Neuroscience*, **22**(1): 7–14.

Hajdarovic KH, Yu DD, Hassell LA, et al. 2022. Single-cell analysis of the aging female mouse hypothalamus. *Nature Aging*, **2**(7): 662–678.

Hajós F, Kálmán M. 1989. Distribution of glial fibrillary acidic protein (GFAP)-immunoreactive astrocytes in the rat brain. II. Mesencephalon, rhombencephalon and spinal cord. *Experimental Brain Research*, **78**(1): 164–173.

Harrison L, Pfuhlmann K, Schriever SC, et al. 2019. Profound weight loss induces reactive astrogliosis in the arcuate nucleus of obese mice. *Molecular Metabolism*, **24**: 149–155.

Heffernan KS, Martinez I, Jaeger D, et al. 2024. Scaled complexity of mammalian astrocytes: insights from mouse and macaque. *Journal of Comparative Neurology*, **532**(8): e25665.

Henneberger C, Bard L, Panatier A, et al. 2020. LTP induction boosts glutamate spillover by driving withdrawal of perisynaptic astroglia. *Neuron*, **108**(5): 919–936. e11.

Herde MK, Bohmbach K, Domingos C, et al. 2020. Local efficacy of glutamate uptake decreases with synapse size. *Cell Reports*, **32**(12): 108182.

Herrera Moro Chao D, Kirchner MK, Pham C, et al. 2022. Hypothalamic astrocytes control systemic glucose metabolism and energy balance. *Cell Metabolism*, **34**(10): 1532–1547. e6.

Hertz L, Chen Y. 2016. Importance of astrocytes for potassium ion (K^+) homeostasis in brain and glial effects of K^+ and its transporters on learning. *Neuroscience & Biobehavioral Reviews*, **71**: 484–505.

Hodge RD, Bakken TE, Miller JA, et al. 2019. Conserved cell types with divergent features in human versus mouse cortex. *Nature*, **573**(7772): 61–68.

Huang ZH, Ni RJ, Luo PH, et al. 2020. Distribution of tyrosine-hydroxylase-immunoreactive neurons in the hypothalamus of tree shrews. *Journal of Comparative Neurology*, **528**(6): 935–952.

Hwang IK, Choi JH, Li H, et al. 2008. Changes in glial fibrillary acidic protein immunoreactivity in the dentate gyrus and hippocampus proper of adult and aged dogs. *Journal of Veterinary Medical Science*, **70**(9): 965–969.

Irala D, Wang SY, Sakers K, et al. 2024. Astrocyte-secreted neurocan controls inhibitory synapse formation and function. *Neuron*, **112**(10): 1657–1675. e10.

Jia J, Chen T, Chen C, et al. 2024. Astrocytes in preoptic area regulate acute nociception-induced hypothermia through adenosine receptors. *CNS Neuroscience & Therapeutics*, **30**(5): e14726.

Kálmán M, Hajós F. 1989. Distribution of glial fibrillary acidic protein (GFAP)-immunoreactive astrocytes in the rat brain. I. Forebrain. *Experimental Brain Research*, **78**(1): 147–163.

Keuker JIH, Rochford CDP, Witter MP, et al. 2003. A cytoarchitectonic study of the hippocampal formation of the tree shrew (*Tupaia belangeri*). *Journal of Chemical Neuroanatomy*, **26**(1): 1–15.

Khakh BS, Deneen B. 2019. The emerging nature of astrocyte diversity. *Annual Review of Neuroscience*, **42**: 187–207.

Khakh BS, Sofroniew MV. 2015. Diversity of astrocyte functions and phenotypes in neural circuits. *Nature Neuroscience*, **18**(7): 942–952.

Lawal O, Ulloa Severino FP, Eroglu C. 2022. The role of astrocyte structural plasticity in regulating neural circuit function and behavior. *Glia*, **70**(8): 1467–1483.

Li HL, Xiang BL, Li X, et al. 2024. Cognitive deficits and Alzheimer's disease-like pathologies in the aged Chinese tree shrew. *Molecular Neurobiology*, **61**(4): 1892–1906.

Liu CY, Si W, Tu CF, et al. 2023. Deficiency of primate-specific *SSX1* induced asthenoteratozoospermia in infertile men and cynomolgus monkey and tree shrew models. *The American Journal of Human Genetics*, **110**(3): 516–530.

Lu JS, Yue F, Liu XQ, et al. 2016. Characterization of the anterior cingulate cortex in adult tree shrew. *Molecular Pain*, **12**: 1744806916684515.

Lu T, Peng HM, Zhong LP, et al. 2021. The tree shrew as a model for cancer research. *Frontiers in Oncology*, **11**: 653236.

Manu DR, Slevin M, Barcutean L, et al. 2023. Astrocyte involvement in blood-brain barrier function: a critical update highlighting novel, complex, neurovascular interactions. *International Journal of Molecular Sciences*, **24**(24): 17146.

Meng XL, Shen F, Li CL, et al. 2016. Depression-like behaviors in tree shrews and comparison of the effects of treatment with fluoxetine and carbetocin. *Pharmacology Biochemistry and Behavior*, **145**: 1–8.

Murphy-Royal C, Gordon GR, Bains JS. 2019. Stress-induced structural and functional modifications of astrocytes-Further implicating glia in the central response to stress. *Glia*, **67**(10): 1806–1820.

Ni RJ, Huang ZH, Luo PH, et al. 2018. The tree shrew cerebellum atlas: systematic nomenclature, neurochemical characterization, and afferent projections. *Journal of Comparative Neurology*, **526**(17): 2744–2775.

Ni RJ, Luo PH, Shu YM, et al. 2016. Whole-brain mapping of afferent projections to the bed nucleus of the stria terminalis in tree shrews. *Neuroscience*, **333**: 162–180.

Ni RJ, Shu YM, Li T, et al. 2021a. Whole-brain afferent inputs to the caudate nucleus, putamen, and accumbens nucleus in the tree shrew striatum. *Frontiers in Neuroanatomy*, **15**: 763298.

Ni RJ, Shu YM, Luo PH, et al. 2015. Immunohistochemical mapping of neuropeptide Y in the tree shrew brain. *Journal of Comparative Neurology*, **523**(3): 495–529.

Ni RJ, Shu YM, Luo PH, et al. 2021b. Whole-brain mapping of afferent projections to the suprachiasmatic nucleus of the tree shrew. *Tissue and Cell*, **73**: 101620.

Ni RJ, Shu YM, Wang J, et al. 2014. Distribution of vasopressin, oxytocin and vasoactive intestinal polypeptide in the hypothalamus and extrahypothalamic regions of tree shrews. *Neuroscience*, **265**: 124–136.

Nie XP, Xu XS, Feng Z, et al. 2024. Depicting primate-like granular dorsolateral prefrontal cortex in the Chinese tree shrew. *eNeuro*, **11**(10): ENEURO.0307–24.2024.

Oberheim NA, Goldman SA, Nedergaard M. 2012. Heterogeneity of astrocytic form and function. *In*: Milner R. Astrocytes: Methods and Protocols. Humana Totowa: Springer, 23–45.

Oberheim NA, Takano T, Han XN, et al. 2009. Uniquely hominid features of adult human astrocytes. *The Journal of Neuroscience*, **29**(10): 3276–3287.

Ota Y, Zanetti AT, Hallock RM. 2013. The role of astrocytes in the regulation of synaptic plasticity and memory formation. *Neural Plasticity*, **2013**: 185463.

Paxinos G, Franklin KBJ. 2001. The Mouse Brain in Stereotaxic Coordinates. 2nd ed. San Diego: Academic Press.

Philippot C, Griemsmann S, Jabs R, et al. 2021. Astrocytes and oligodendrocytes in the thalamus jointly maintain synaptic activity by supplying metabolites. *Cell Reports*, **34**(3): 108642.

Qi XH, Chen P, Wang YJ, et al. 2024. Increased cysteinyl-tRNA synthetase drives neuroinflammation in Alzheimer's disease. *Translational Neurodegeneration*, **13**(1): 3.

Rahimian R, Perlman K, Fakhfouri G, et al. 2024. Proteomic evidence of depression-associated astrocytic dysfunction in the human male olfactory bulb. *Brain, Behavior, and Immunity*, **122**: 110–121.

Rajkowska G, Stockmeier CA. 2013. Astrocyte pathology in major depressive disorder: insights from human postmortem brain tissue. *Current Drug Targets*, **14**(11): 1225–1236.

Sardar D, Cheng YT, Woo J, et al. 2023. Induction of astrocytic Slc22a3 regulates sensory processing through histone serotonylation. *Science*, **380**(6650): eade0027.

Schitine C, Nogaroli L, Costa MR, et al. 2015. Astrocyte heterogeneity in the brain: from development to disease. *Frontiers in Cellular Neuroscience*, **9**: 76.

Schwerdtfeger WK. 1984. Structure and fiber connections of the hippocampus. A comparative study. *Advances in Anatomy, Embryology, and Cell Biology*, **83**: 1–74.

Shu YM, Ni RJ, Sun YJ, et al. 2015. Distribution of corticotropin-releasing factor in the tree shrew brain. *Brain Research*, **1618**: 270–285.

Sonnay S, Poirot J, Just N, et al. 2018. Astrocytic and neuronal oxidative metabolism are coupled to the rate of glutamate-glutamine cycle in the tree shrew visual cortex. *Glia*, **66**(3): 477–491.

Stogsdill JA, Ramirez J, Liu D, et al. 2017. Astrocytic neuroligins control astrocyte morphogenesis and synaptogenesis. *Nature*, **551**(7679): 192–197.

Tsukiyama-Kohara K, Kohara M. 2014. *Tupaia belangeri* as an experimental animal model for viral infection. *Experimental Animals*, **63**(4): 367–374.

Ung K, Huang TW, Lozzi B, et al. 2021. Olfactory bulb astrocytes mediate sensory circuit processing through Sox9 in the mouse brain. *Nature Communications*, **12**(1): 5230.

Ung K, Tepe B, Pekarek B, et al. 2020. Parallel astrocyte calcium signaling modulates olfactory bulb responses. *Journal of Neuroscience Research*, **98**(8): 1605–1618.

Vasile F, Dossi E, Rouach N. 2017. Human astrocytes: structure and functions in the healthy brain. *Brain Structure and Function*, **222**(5): 2017–2029.

Venkateshappa C, Harish G, Mythri RB, et al. 2012. Increased oxidative damage and decreased antioxidant function in aging human substantia nigra compared to striatum: implications for Parkinson's disease. *Neurochemical Research*, **37**(2): 358–369.

Ventura R, Harris KM. 1999. Three-dimensional relationships between hippocampal synapses and astrocytes. *The Journal of Neuroscience*, **19**(16): 6897–6906.

Verkhratsky A, Matteoli M, Parpura V, et al. 2016. Astrocytes as secretory cells of the central nervous system: idiosyncrasies of vesicular secretion. *The EMBO Journal*, **35**(3): 239–257.

Walz W. 2000. Controversy surrounding the existence of discrete functional classes of astrocytes in adult gray matter. *Glia*, **31**(2): 95–103.

Walz W, Lang MK. 1998. Immunocytochemical evidence for a distinct GFAP-negative subpopulation of astrocytes in the adult rat hippocampus. *Neuroscience Letters*, **257**(3): 127–130.

Wang J, Xu XL, Ding ZY, et al. 2013. Basal physiological parameters in domesticated tree shrews (*Tupaia belangeri chinensis*). *Zoological Research*, **34**(E2): E69–E74.

Wang J, Zhou QX, Tian M, et al. 2011. Tree shrew models: a chronic social defeat model of depression and a one-trial captive conditioning model of learning and memory. *Zoological Research*, **32**(1): 24–30.

Xiao J, Liu R, Chen CS. 2017. Tree shrew (*Tupaia belangeri*) as a novel laboratory disease animal model. *Zoological Research*, **38**(3): 127–137.

Yao YG. 2017. Creating animal models, why not use the Chinese tree shrew (*Tupaia belangeri chinensis*)?. *Zoological Research*, **38**(3): 118–126.

Yao YG, Lu L, Ni RJ, et al. 2024. Study of tree shrew biology and models: a booming and prosperous field for biomedical research. *Zoological Research*, **45**(4): 877–909.

Zhao YQ, Liu YQ, Yuan JF, et al. 2018. Regeneration of islet β-cells in tree shrews and rats. *Animal Models and Experimental Medicine*, **1**(2): 152–161.

Zhou B, Zuo YX, Jiang RT. 2019. Astrocyte morphology: diversity, plasticity, and role in neurological diseases. *CNS Neuroscience & Therapeutics*, **25**(6): 665–673.

Zhou JN, Ni RJ. 2016. The Tree Shrew (*Tupaia Belangeri Chinensis*) Brain in Stereotaxic Coordinates. Singapore: Springer.